Cation Control of Cooperative CO_2 Adsorption in Li-containing Mixed Cation forms of the Flexible Zeolite Merlinoite

Veselina M. Georgieva,[1,†] Elliott L. Bruce,[1,†] Ruxandra G. Chitac,[1] Magdalena M. Lozinska,[1] Anna M. Hall,[1] Claire A. Murray,[2] Ronald I. Smith,[3] Alessandro Turrina[4] and Paul A. Wright[1,*]

[1] EaStCHEM School of Chemistry, University of St Andrews, Purdie Building, North Haugh, St Andrews, KY16 9ST, UK. Email: paw2@st-andrews.ac.uk

[2] Diamond Light Source, Harwell Science and Innovation Campus, Didcot, OX11 0DE, UK

[3] ISIS Neutron and Muon Source, Rutherford Appleton Laboratory, Harwell Campus, Didcot, OX11 0QX, UK

[4] Johnson Matthey Technology Centre, Chilton P.O. Box 1, Belasis Avenue, Billingham TS23 1LB, UK

† These authors contributed equally

Abstract

The lithium-exchanged form of a merlinoite zeolite (MER) with Si/Al = 4.2 (unit cell composition $Li_{6.2}Al_{6.2}Si_{25.8}O_{64}$) possesses a strongly contracted framework when dehydrated (the unit cell volume decreases by 12.9% from the hydrated 'wide-pore' form to the dehydrated 'narrow-pore' form). It shows cooperative adsorption behaviour for CO_2, leading to two-step isotherms with the second step at elevated pressure (>2.5 bar at 298 K). Partially exchanging Na and K cations to give single phase Li,Na- and Li,K-MER materials reduces the pressure of this second adsorption step because the transition from narrow- to wide-pore forms upon CO_2 adsorption occurs at lower partial pressures compared to that in Li-MER: partial exchange with Cs does not reduce the pressure of this transition. Exsolution effects are also seen at K cation contents >2.2 per unit cell. The phase transitions proceed *via* intermediate structures, by complex phase behaviour rarely seen for zeolitic materials. The strongly distorted narrow-pore structures adopted upon dehydration give one dimensional channel structures in which the

percolation of CO_2 through the material requires cation migration from their locations in *ste* sites. This is slow in $Li_{3.4}Cs_{2.8}$-MER where Cs cations occupy these critical *ste* cavities in the channels, causing very slow adsorption kinetics. As the partial pressure of CO_2 increases, a threshold pressure is reached where cooperative adsorption and Cs cation migration occur and the wide-pore form results, with a three dimensionally connected pore system, leading to a sharp increase in uptake. This is far in excess of the increase of unit cell volume because more of the pore space becomes accessible. Strong hysteretic effects occur upon desorption, leading to CO_2 encapsulation. CO_2 remaining within the material after repeated adsorption/desorption cycles without heated activation improves sorption kinetics and modifies the stepped isotherms.

Introduction

Zeolites find wide-ranging application in commercially-important gas separations, including N_2 from O_2 in air and CO_2 from H_2.[1-6] The latter is important in purification of H_2 from methane reforming or from CH_4 in natural gas and biogas upgrading. In most of these processes the high selectivity arises from the difference in interaction of the molecular adsorbates with extra-framework cations, although molecular sieving can enhance the equilibrium selectivity in small pore zeolites *via* kinetic effects.[7–11] Small pore refers here to openings of 4 Å or less, usually comprising eight-membered rings (8Rs) built from 8 tetrahedral cations (Si/Al) and 8 O atoms.

Adsorption on alkali metal cation forms of important zeolites such as A, chabazite and X (topology types LTA, CHA and FAU[12]) has been studied extensively and clear trends have been observed for cations of different ionic radii (from Li^+ (0.76 Å) to Cs^+ (1.67 Å)).[7,13-15] The size of the cations controls their interaction strength with adsorbates,[16-18] as well as their preference for different sites in the zeolite pores, where they coordinate to framework O atoms. In Li,Na-CHA, for example, the Li cations prefer 6R sites, whilst larger Na cations are then located in 8R sites.[19] As a consequence of the high charge density of Li^+, Li-forms of zeolites X and chabazite have attractive properties, for example in the separation of N_2 from O_2 by virtue of the higher polarizability of N_2.[20,21] The strong influence of Li^+ is illustrated in zeolite Li,Na-LSX (LSX = low silica X), where an optimum uptake of N_2 is achieved at Li^+ contents above 67 cations per unit cell.[22] This is because Li^+ prefers 6R sites in the β-cages of X, where it is inaccessible to adsorbates, leaving Na cations in the supercage sites. Only above a certain Li^+ exchange level are the accessible sites in the supercages filled by Li^+.

The majority of investigations of the structures of cationic forms of zeolites and their adsorption properties consider the frameworks rigid, with cations held in sites of fixed geometry. The adsorption isotherms are generally Type I in the IUPAC nomenclature, where the uptake asymptotes toward a maximum value as the pores are progressively filled. Recently, however, the study of adsorption of the polar adsorbate CO_2 on cation forms of flexible zeolites - those that possess frameworks that can change configuration via complex coordinated tilting of their rigid tetrahedral building units - has revealed adsorption behaviour that is not Type I in character. Instead, their isotherms may be convex to the pressure axis or display inflections and steps.[23-25] Furthermore, CO_2 uptake is observed in zeolites where crystallography indicates full cation occupancy of window sites, requiring motion of these cations to allow molecular diffusion.[8,10,26] Such 'exotic' behaviour has for some time been appreciated as a feature of many metal-organic framework (MOF) materials,[27,28] where tilts and rotations of the organic linkers give rise to marked 'breathing' effects (including major increases in unit cell volumes and adsorption capacity) and 'gating' behaviour, but it has not been widely recognised in zeolites.

These 'breathing' and 'gating' effects result from the dynamic behaviour of the adsorbent structure during gas uptake. For zeolites this can be movement of the cations or distortion of the aluminosilicate framework away from its relaxed, lowest energy configuration.[23-25,29] Cations can temporarily move away from window sites where they obstruct or block access to pore space, giving rise to gating effects, and the configuration of the framework itself can change in response to cation migration. Cation gating has been demonstrated in several small pore zeolites with low Si/Al ratios, including Rho and chabazite, where blocking cations move away from 8R sites with sufficient frequency to allow highly selective passage of CO_2 before returning to the window site.[25,29-31] Such behaviour need not give non-Type I isotherms, but strongly non-Type I behaviour is observed when there is an accompanying structural change that results in the adsorption affinity increasing with uptake. This gives isotherms that increase in steepness over some regions of increasing pressure. Analogous 'cooperative' effects are observed for ligand binding to proteins, such as CO_2 on the photosynthetically-relevant Rubisco enzyme.[32] This is in turn taken as a model for the strongly stepped CO_2 isotherms observed on diamine-appended Mg_2(dobpdc) MOFs of Long *et al*. (dopbdc = dioxyibiphenyldicarboxylate).[33] The potential for stepped isotherms to facilitate enhanced working capacities over narrow pressure ranges is underlined by the great current interest in amine-loaded MOFs for carbon capture applications.[34,35]

Zeolite Rho and higher members of the extended RHO family of small pore zeolite structures have been observed to give CO_2 isotherms with noticeable inflections and steps when suitably cation exchanged (Na- and Cs-Rho, Na- and Cs-forms of ZSM-25 and PST-20, for example).[36-39] For Cs-Rho, there is slow movement of Cs cations from D8R to S8R sites that results in a sluggish change of phase and increase in uptake, while in ZSM-25 there is a stepped increase in uptake that offers appreciable CO_2 uptake over a narrow pressure range. ZSM-25 displays a reversible unit cell volume increase related to the adsorption step, but the framework is too complex for the structural mechanism to be fully resolved.

More recently, studies of the flexible small-pore zeolites merlinoite and gismondine have revealed strongly non-Type I CO_2 isotherms.[23-25] In these cases, the relatively simple structures have enabled the structural mechanisms of this cooperative behaviour to be established. In each case the framework structure transforms to a narrow pore form upon dehydration. In this way the framework O atoms achieve optimum electrostatic interaction with the extra-framework cations, although at the cost of some energy required to distort the framework. CO_2 adsorption on the dehydrated zeolite initially occurs with a reduced affinity (and Henry Law constant) because the cations are initially closely bound to the framework and relatively inaccessible. Progressive uptake results in the cations moving away from the framework and becoming more accessible. This leads to the framework expanding to the wide pore forms, which have greater CO_2 capacity. The structure of merlinoite, the subject of this work, is shown in Figure 1 (with undistorted framework and cation sites).

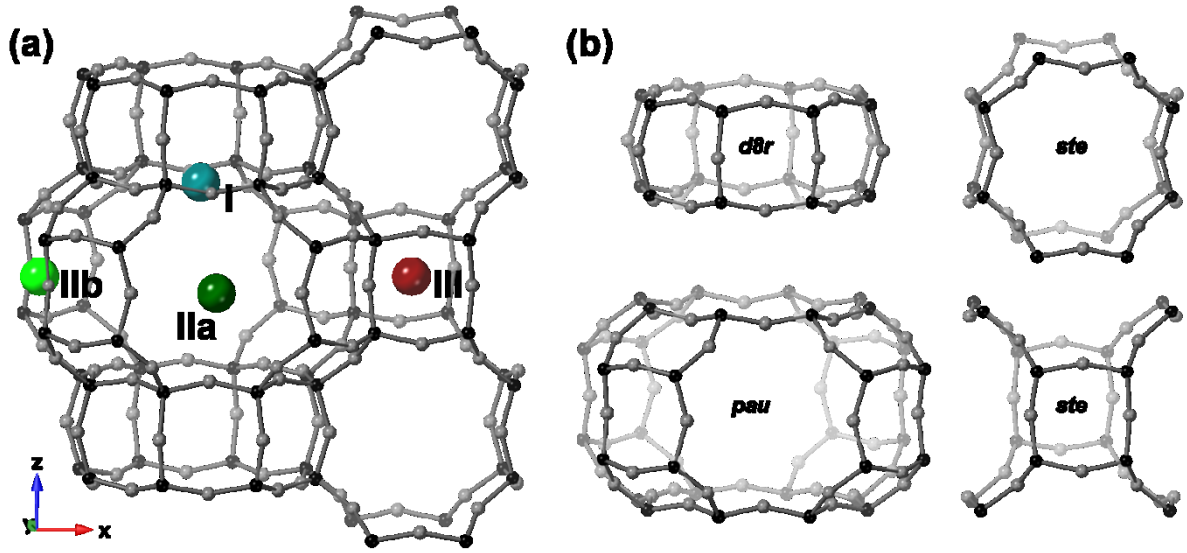

Figure 1. The framework structure of MER with (a) labelling schemes used here for cation sites and (b) component cavities. Tetrahedral cation sites and O sites are shown in black and grey, respectively.

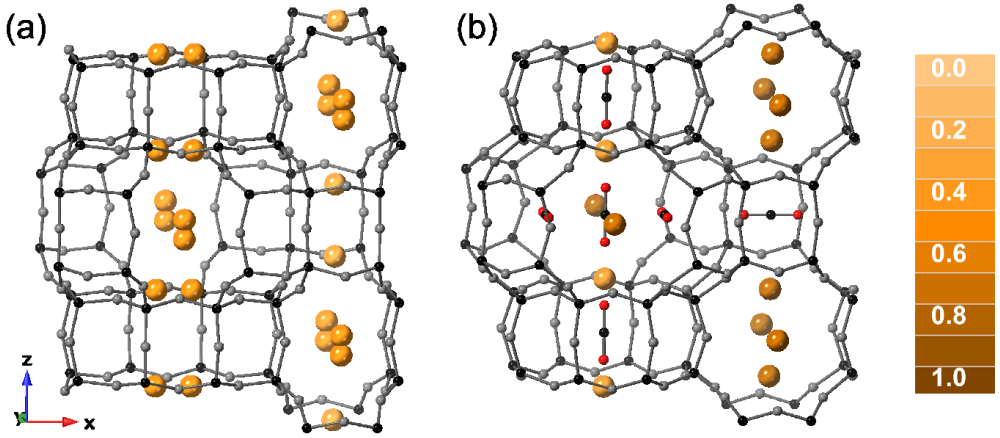

Figure 2. Framework structures of Na-MER (3.8) upon (a) dehydration and (b) subsequent exposure to CO_2. T and O sites are shown in black and grey, respectively. Na cations are shown in varying shades of orange, with lightness indicating fractional occupancy, as described on the right. CO_2 molecules are shown in black and red.[23]

In our studies of merlinoite (MER) with a Si/Al ratio of 3.8, we observed a narrow-to-wide pore transition for Na-, K- and Cs-forms. The mechanism of opening varies strongly between the different cation forms, in terms of equilibrium position, kinetics, and structural mechanism. In Na-MER, for example, the transition is gradual and sluggish, and requires close to 1 bar CO_2 at 298 K, whereas in K-MER it occurs rapidly and at very low CO_2 pressure. Figure 2 illustrates the structural change observed upon uptake of CO_2 on Na-MER, for example. The 8R windows become less elliptical, and there are important movements of Na cations between sites. The Cs-

form displays stepped isotherms and also achieves the wide pore state at relatively low CO_2 pressures at 298 K. There is migration of cations from D8R sites and *ste* cavities to S8R sites: this occurs as the coordination geometry of the sites changes when the structure undergoes transition to the wide pore form.

Very recently, Choi et al.[25] have investigated the CO_2 adsorption behaviour of merlinoite further. In particular, in measurements up to 1 bar, they have shown that Na, K, Rb and Cs-merlinoites with a lower Si/Al framework ratio (2.3) show strong cation gating effects (where cations have to move from windows to allow CO_2 to pass) because of the high cation contents. Their CO_2 adsorption isotherms are observed to show temperature-dependent steps, due to the cooperative narrow-wide pore transition.

It is not possible to investigate the CO_2 adsorption of Li-forms of MER with Si/Al of 3.8 or lower because they lose crystallinity upon dehydration. A similar problem of lowered stability in the Li-form has been reported for chabazite.[19] However, merlinoite with a higher Si/Al ratio (4.2) has been prepared and the fully Li-exchanged form of this zeolite is stable to dehydration, upon which it gives a narrow pore material with a strongly contracted framework. Here we report the adsorption behaviour of this lithium merlinoite, Li-MER, and its mixed cation derivatives.

Li-MER transforms to the wide pore form only at elevated CO_2 pressure at room temperature but exhibits significant porosity even in the strongly contracted narrow-pore form. We aimed to reduce the opening pressure by preparing mixed cation forms in which the Li^+ has been partially replaced by larger Na, K and Cs cations, because those forms are known to open at pressures below 1 bar. Effective control of the pressure of an isotherm step could find application in tailored adsorbents. Here we report the CO_2 adsorption properties of these materials and their structures with and without adsorbed CO_2. A remarkable range of phenomena was observed: cation site ordering and exsolution; cation migration and gating during CO_2 adsorption; strongly non-Type I adsorption behaviour accompanying pore opening; and hysteresis leading to CO_2 'encapsulation'. These effects result from finely balanced framework-cation and cation-CO_2 interactions and important changes of cation site geometry that result from the framework expansion.

Experimental

Exchange of MER Zeolites

K,TEA-MER with a Si/Al ratio of 4.2 was provided from Johnson Matthey. The as-prepared K,TEA-MER was heated at 823 K under oxygen for 12 h to remove the template (denoted K,H-MER). The calcined zeolite was repeatedly exchanged with 10% nitrate solutions of Li, Na, K and Cs (99.5-99.9%; Sigma-Aldrich) at 353 K in a round bottom flask with a condenser. In all cases, cation exchange was repeated until EDX analysis indicated the exchange was complete. A second cation exchange was performed into these monovalent cation forms of MER zeolite by varying the concentration of Li nitrate solutions (99% Sigma-Aldrich). The $Li_xNa_{6.2-x}[Al_{6.2}Si_{25.8}O_{64}]$ series, where x is close to the integer values 1-5, was prepared from 0.3 g of Na-MER, stirred in 200 mL of different concentrations of Li nitrate solution at 378 K for 5 h. Specifically, $Li_{4.0}K_{2.2}$-MER was prepared *via* 3 consecutive ion exchanges of 0.3 g K,H-MER with 200 mL, 5 wt% $LiNO_3$ solution for 5 h at 378 K. Similarly, $Li_{3.4}Cs_{2.8}$-MER was prepared from 0.3 g of Cs-MER with 200 mL, 5 wt% $LiNO_3$ solution for 3 h at 378 K. All ion-exchanged samples were washed with water and dried overnight at 378 K prior to any characterisation. EDX analysis of all samples was performed in a JEOL JSM 5600 SEM with an Oxford INCA Energy 200 EDX analyser. To confirm the concentration of lithium in selected samples, ICP analysis on filtrate from repeated ion exchange of samples was performed (Supporting Information, Table S1).

Characterisation

Powder X-ray diffraction (PXRD) patterns of all Li-containing MER samples were measured at 298 K in the hydrated and dehydrated forms. In order to measure the structure of dehydrated zeolites, the powders were loaded into 0.7 mm quartz glass capillaries to a depth of around 2 cm and heated for 16 h at 623 K under a vacuum of 10^{-5} mbar on a glass line. After full dehydration, all capillaries were flame sealed under vacuum. The powder X-ray diffraction patterns of all hydrated and dehydrated samples were measured in Debye−Scherrer geometry on a Stoe STAD i/p diffractometer using Cu $K\alpha_1$ X-rays (1.54056 Å) except $Li_{4.0}K_{2.2}$-, $Li_{3.7}K_{2.5}$- and $Li_{3.4}Cs_{2.8}$-MER which were analysed by synchrotron X-ray diffraction at I11 at Diamond Light Source, Oxfordshire (0.826398 Å) using the Mythen position sensitive detector.

Neutron powder diffraction (PND) was performed on a dehydrated sample of the $Li_{6.2}$-MER material. Prior to the neutron diffraction experiment, a 3 grams batch of $Li_{6.2}$-MER zeolite was dehydrated on a glass line at 573 K under high vacuum (5×10^{-5} mbar) for 5 days. The

dehydrated sample was packed in an 8 mm diameter vanadium can in a glove box and sealed using an indium wire. Time-of-flight neutron powder diffraction data were recorded on the Polaris diffractometer the ISIS Neutron and Muon Source, Rutherford Appleton Laboratory, Didcot, UK.[40] Measurement was performed on the dehydrated sample at ambient conditions. Diffraction patterns were collected simultaneously in 5 discrete detector banks centred at 2θ scattering angles of 10.40° (bank 1), 25.99° (bank 2), 52.21° (bank 3), 92.59° (bank 4) and 146.72° (bank 5).

To observe the structural changes during CO_2 adsorption on MER samples, *in situ* X-ray powder diffraction was performed on a PANalytical Empyrean diffractometer with a Mo X-ray tube with a ß-filter (giving Mo $K_{\alpha 1,2}$ X-rays) and an X'celerator RTMS detector. The instrument was equipped with an Anton Paar HTK1200N stage (from room temperature to 1100 K, up to 1 bar pressure of inert/reducing gas), working in reflection, Bragg−Brentano, θ−θ mode. First, the sample was placed on an alumina disk and inserted in a cell, equipped with a furnace. The sample was evacuated and degassed at 573 K for 8 h under a vacuum of 10^{-6} mbar. The furnace was connected to a gas handling rig and CO_2 was dosed via a needle valve. The pressure was followed on a RS PRO vacuum gauge with a maximum pressure measurement of 0 bar overpressure (1 bar absolute pressure). Series of diffraction patterns, each of 60 min and over the 2θ range 3.5−25°, were collected at 298 K before and after dehydration and also after dosing with 0.02, 0.10, 0.20, 0.30, 0.40, 0.60, 0.70, 0.80, and 1.0 bar CO_2, each time after 30 min equilibration.

The structural response to CO_2 adsorption of $Li_{3.4}Cs_{2.8}$-MER was measured at I11 at the Diamond Light Source (0.826398 Å). The sample was loaded into a 0.7 mm silica glass capillary to a depth of around 1 cm and a silica wool plug was packed above this to prevent loss of powder upon evacuation and dehydration. The capillary was attached to a gas dosing line attached to a goniometer head, which was permitted to rock by 20° in the beam to improve powder averaging during diffraction. The sample was dehydrated under evacuation (10^{-5} mbar) for 1 – 2 h using an Oxford Cryocool blowing hot air at 500 K plus intermittent use of a hot air blower. Series of diffraction patterns, each of 2 minutes and over the 2θ range 2 – 90°, were collected at 298 K before and after dehydration, and also after dosing with CO_2, each time after 10-20 minutes. Measurements were made using the Mythen position sensitive detector. This gave excellent signal to noise in very short collection times and is the detector of choice for these measurements on our samples. The pressure of CO_2 was increased stepwise from 0.02 to 5 bar, and then removed by evacuation, either fully or in some cases partially, to measure the

isotherms on the desorption branch of the isotherm. In this way, PXRD data was collected that was suitable for analysis by Rietveld refinement, details of which are given in the Crystallography section and in the SI. It should be noted that the Li,Cs-MER that was analysed by refinement had been held at pressures of >2.5 bar for 1 h to reach equilibrium.

High-pressure CO_2 adsorption isotherms were measured from 0 to 5 bar at 298 K using a Hiden IGA gravimetric analyser using ~20 mg of sample, which was outgassed at 573 K under vacuum for 10 h before each adsorption experiment. The temperature of the sample was subsequently reduced under vacuum until the target temperature (between 298 and 328 K) was reached. The mass change for each adsorption/desorption step was followed, and a final reading was taken when it had reached 98% of the asymptoted equilibrium value or after 90 min, whichever was shorter. For the $Li_{3.4}Cs_{2.8}$-MER sample, repeated CO_2 adsorption and desorption cycles were measured. After the first cycle, the sample was kept in vacuum and outgassed for 4 hours at 298 K until the pressure reached 7.10^{-7} mbar at the vacuum gauge, and a second experiment was then executed at 298 K. This procedure was repeated 15 times, with outgassing of the sample prior to the final experiment at 523 K under vacuum for 10 h.

Crystallography

Most structures were determined by Rietveld refinement against PXRD data using TOPAS Academic software.[41] Starting framework models were adapted from literature examples with the unit cell modified to that derived from the diffraction pattern. The *Immm* space group gave the best fits in all cases. Starting cation positions were estimated from literature models, and geometric restraints on T−O and O−O distances of 1.63 and 2.66 Å, respectively, were used to maintain regular tetrahedral coordination. Modified Thompson-Cox-Hastings pseudo-Voigt "TCHZ" peak profiles gave the best fit of those available. Final extraframework cation positions and occupancies were determined by refinement of starting positions and through the use of difference Fourier mapping. The latter was used to determine the positions of water and CO_2 molecules in hydrated and CO_2-loaded samples, respectively. Water molecules were modelled as a single O whilst CO_2 molecules were treated as rigid bodies, with final positions and occupancies determined by refinement. Li cations were not included in refinement models as confident site positions and occupancies were not possible.

To determine the position of Li cations in dehydrated $Li_{6.2}$-MER, a multidataset refinement was conducted for the neutron diffraction data on independent banks 3, 4 and 5 using the GSAS software.[42,43] The neutron scattering length of lithium (-1.9 fm) is significant (and of different sign) compared to those of Al, Si and O (3.5, 4.1 and 5.8 fm, respectively). Resolution of the very low angle banks 1 and 2 was too low to warrant inclusion in the refinement. The structural model from the Rietveld refinement with PXRD data was used as a starting model for the time-of-flight powder neutron diffraction data. The background for all patterns was fitted by a 20-36 term shifted Chebyshev function. The framework atomic positions were initially refined with geometric restraints on T-O (T = Si or Al; 1.60 ± 0.02 Å) and O-O (2.60 ± 0.02 Å) distances to maintain regular tetrahedral coordination. Difference Fourier methods were used to look for extra framework cation sites. Finally, the framework restraints were gradually removed.

Details of all the XRD and neutron diffraction and refinements are given in the SI (Section 2, Figures S2-S16, S18-S19, Tables S2-S18).

Computational work

All calculations were carried out using BIOVIA Materials Studio 2020.[44] All energy and geometry optimisation calculations were carried out using the COMPASS II forcefield. 2×2×2 all-silica supercells were used in all calculations and their framework structures were obtained from Rietveld refinements of the dehydrated $Li_{6.2}$-MER (representative of the narrow pore structure) and the $Li_{3.8}Cs_{2.4}$-MER (representative of the wide-pore structure). Additionally, an attempt was made to model the effect of charged cations on the adsorption. For the narrow Li-MER structure, 48 Li^+ cations were spread over the two sites found in the Rietveld refinement (35 cations in Site I and 13 in Site II), with the charge from these cations balanced by negative charge spread over the whole framework. Otherwise, the charges on all atoms were forcefield assigned. For the $Li_{3.8}Cs_{2.4}$-MER structure, only the Cs cations were included, because the positions of Li cations could not be determined in the presence of CO_2 molecules. Nineteen Cs cations were positioned in sites determined from Rietveld refinement and the charge from these cations balanced as before, with the charges on all atoms being forcefield assigned.

Solvent surfaces were plotted on the empty silicate frameworks using the 'Atom Volumes and Surfaces' tool, with a solvent probe radius of 1.15 Å. The van der Waals radii for Si and O were set to 0.5 Å and 1.35 Å, respectively.

The adsorption isotherms were determined with the 'Sorption' module. A geometry optimised CO_2 molecule was used as the sorbate molecule. The geometry optimisation was carried out with the 'Forcite' module, using the Smart algorithm and medium convergence criteria. For each system studied, two 'Adsorption isotherm' calculations were set up – one for pressures between 10^{-4} kPa and 10 kPa in 10 steps, and the second one for pressures between 20 kPa and 500 kPa in 48 steps. The temperature was set to 298 K for all calculations. At each pressure step a Monte Carlo (MC) simulation was performed with the Metropolis method. For each pressure step, the number of equilibration steps was set to 10^5 or 10^6 and the number of production steps was set to 10^6 or 10^7. The higher number of equilibration steps and production steps was needed for structures that contained Li^+ cations. The relative probabilities of the exchange, rotate, translate and regrowth steps of the MC simulation were 2:1:1:0.1.

Results

We have prepared and structurally characterised the activated adsorbent forms of selected series of Li-containing MER materials, and have measured their CO_2 adsorption properties up to 5 bar. We have also followed structural changes by *in situ* diffraction during adsorption. In this section we analyse and report this data for the different samples. However, it is instructive to bring these observations together to get a deeper understanding of the cooperative phenomena that result from the flexibility of the $Al_{6.2}Si_{25.8}O_{64}$ MER framework that is common to all samples, and we do this in the Discussion.

Structural Characterisation of Dehydrated Li,M-Merlinoites

Li-MER ($Li_{6.2}Al_{6.2}Si_{25.8}O_{64}$) was prepared by exhaustive exchange of a K,H-MER material with aqueous Li nitrate solution, as discussed in the experimental section, until no K^+ remains. Unlike Li-MER(3.8) samples, this material remained crystalline after dehydration and subsequent rehydration, as shown by the PXRD patterns in Figure 3a.

Rietveld analysis of the PXRD data for the dehydrated materials (Figure S5, SI) was successfully achieved in the *Immm* space group, which we have previously found to be preferred for merlinoite that contains small cations.[23] It was possible to determine the framework configurations, which are shown in Figures 3b and c, but not the cation sites, due to the low X-ray scattering of Li^+. A small amount of scattering found at the centre of the *pau* cavity in 'dehydrated' Li-MER was fitted as O atoms of residual water. There is a 12.9% decrease of the unit cell volume upon dehydration (Table 1), giving a smaller unit cell size than observed with dehydrated Na-, K- and Cs-forms of MER(3.8) (given in Table 1 for comparison). The free dimensions of 8R openings along the *a*, *b* and *c* directions (crystallographic O - O distances minus 2.7 Å, twice the van der Waals radius of O) are only 3.0, 1.4 and 1.1 Å, respectively (Table 2).

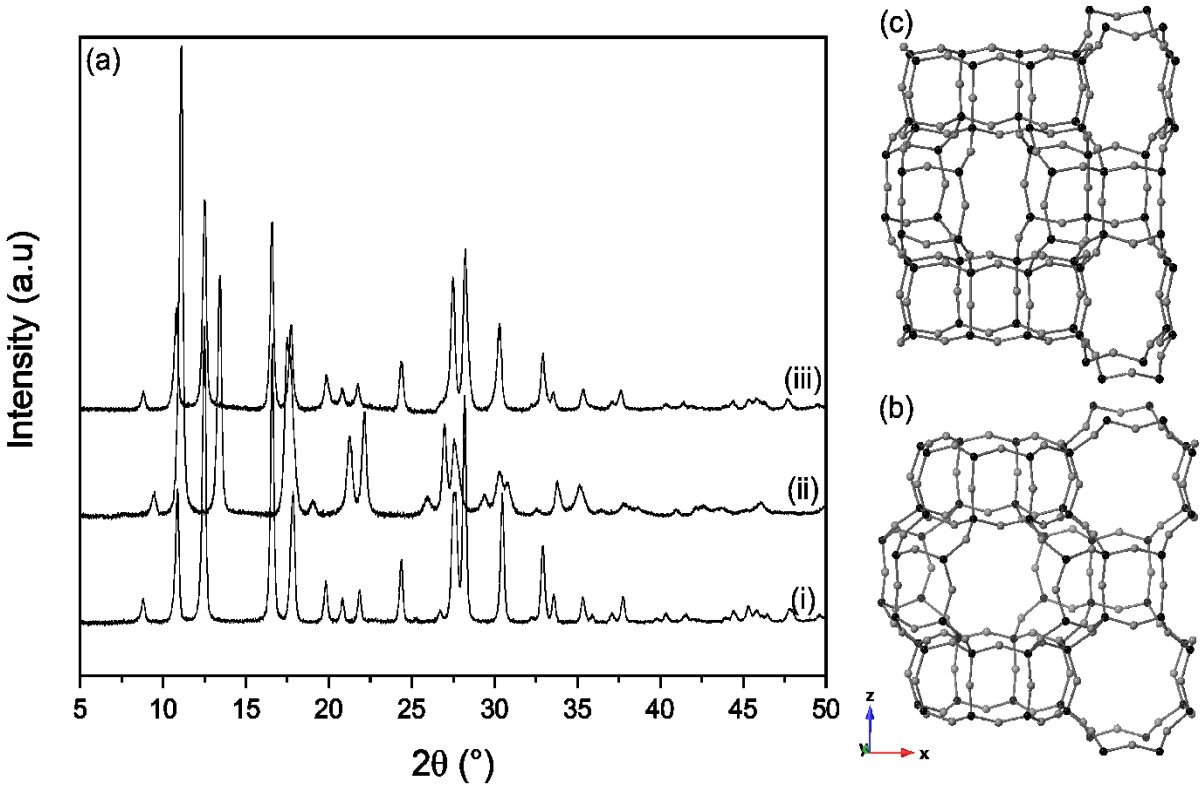

Figure 3. (a) PXRD patterns of Li-MER in (i) hydrated, (ii) dehydrated and (iii) rehydrated forms (λ = 1.54056 Å). (b,c) The framework structures of hydrated and dehydrated Li-MER, respectively. T (Si,Al) and O sites are shown in black and grey, respectively. Backgrounds have been removed to allow comparison of XRDs collected in flat plate and capillary mode.

Neutron powder diffraction and Rietveld refinement were performed to locate the Li cation positions in Li-MER and so to determine the origin of the strong contraction of the framework (See Figures S15 and S16, Tables S16, S17). The strong distortion of the MER framework

observed from PXRD was confirmed (*Immm*, a = 13.1589(11) Å, b = 13.0652(10) Å, c = 9.9754(8) Å, Figure 4). Lithium ions occupy two extra-framework sites. The favoured location, which exhibits maximum possible occupancy, was in site I, in the narrow single 8R site of the *d8r* units, off-centre. Here the Li cation is close to four O atoms, two at 2.19 Å and 2 at 2.23 Å. This site accounts for 4 of the *ca*. 6 Li cations – the others are found, with partial occupancy, within one of the two kinds of *ste* cages. They are in the *ste* cages including the 4Rs at the 'narrow part' of the *d8r* unit, where it achieves close coordination to four O atoms (two at 2.03 Å and two at 2.15 Å). Computational simulations (details in the SI) confirm that the favoured site of Li cations is in site I. This is consistent with the literature, where it has been reported that Li cations typically sit in sites such as 6Rs[38,45-47] or narrow 8R windows. [8,47]

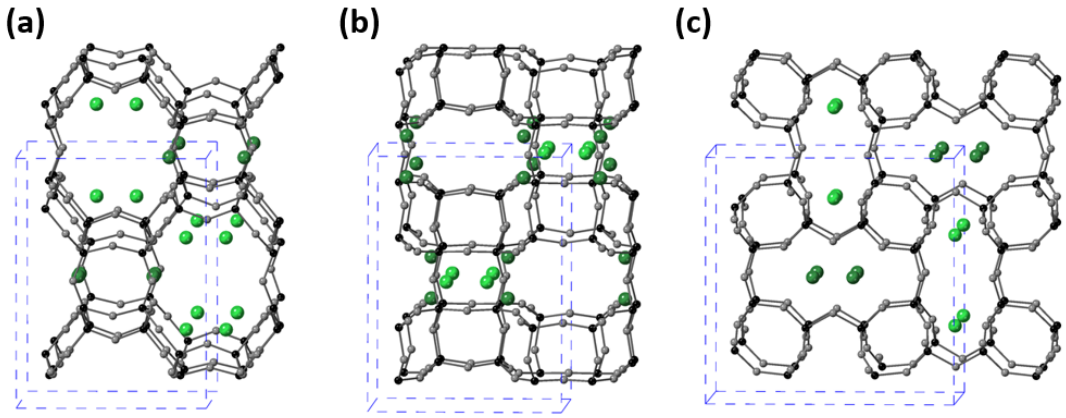

Figure 4. Extended structure of $Li_{6.2}$-MER as viewed down a, b and c axes, respectively. T and O sites are shown in black and grey, with Li^+ shown in shades of green (Site I, dark green; ste site, light green – see text for details).

*Table 1. Unit cell parameters and volumes for Li- and Li,M-MER samples, with space groups (SG) and Rietveld R_{wp} and χ^2 values. (dh), (h) and (ads) indicate dehydrated, hydrated and CO_2 loaded samples, respectively. * MER (3.8) materials reported by Georgieva et al.[23] shown for comparison.*

Sample	SG	*a* (Å)	*b* (Å)	*c* (Å)	*V* (Å^3)	R_{wp}	χ^2
$Li_{6.2}$-MER (dh)	*Immm*	13.206(1)	13.141(1)	9.976(1)	1731.2(2)	3.5%	1.8
$Li_{6.2}$-MER (h)	*Immm*	14.150(1)	14.145(1)	9.926(1)	1986.7(2)	6.4%	2.6
$Li_{5.0}Na_{1.2}$-MER (dh)	*Immm*	13.240(1)	13.172(1)	9.985(1)	1741.3(2)	4.6%	1.6
$Li_{4.0}Na_{2.2}$-MER (dh)	*Immm*	13.297(1)	13.263(1)	9.946(1)	1754.1(3)	4.1%	1.7
$Li_{3.0}Na_{3.2}$-MER (dh)	*Immm*	13.339(1)	13.343(1)	9.948(1)	1770.6(2)	4.1%	1.6
$Li_{5.0}K_{1.2}$-MER (dh)	*Immm*	13.225(1)	13.179(1)	9.938(1)	1732.2(2)	4.5%	2.2
$Li_{4.0}K_{2.2}$-MER (dh)	*Immm*	13.275(1)	13.244(1)	9.907(1)	1741.7(2)	2.9%	5.5
$Li_{3.4}Cs_{2.8}$-MER (dh)	*Immm*	13.337(1)	13.377(1)	9.837(1)	1755.0(2)	3.0%	5.8
$Li_{3.4}Cs_{2.8}$-MER (h)	*Immm*	14.153(1)	14.154(1)	10.003(1)	2003.8(2)	4.7%	9.3
$Li_{3.4}Cs_{2.8}$-MER (ads)	*Immm*	14.088(1)	14.099(1)	10.028(1)	1991.8(2)	3.3%	6.5
$Na_{6.7}$-MER (dh)*	*Immm*	13.493(1)	13.520(1)	9.914(1)	1809(1)	8.2%	1.3
$K_{6.7}$-MER (dh)*	*P*4$_2$/*nmc*	13.586(1)	-	9.876(1)	1823(1)	8.1%	1.6
$Cs_{6.2}K_{0.5}$-MER (dh)*	*P*4$_2$/*nmc*	13.751(1)	-	9.950(1)	1881(1)	9.3%	1.4

Initial CO_2 adsorption measurements at 298 K, described in detail later, showed a stepped 'Type IV' adsorption isotherm. Up to 2.5 bar the uptake is only ~2.5 mmol g^{-1} and only above this pressure does the uptake increase to values expected for the wide pore form on the basis of previous experiments. Na-MER(3.8) was observed to take up *ca*. 5 mmol g^{-1} at 5 bar, for example. This indicated that the narrow-to-wide pore transition in Li-MER does not take place below 2.5 bar. To investigate whether this transition could be shifted to lower pressure, mixed cation Li,M-MER (M-Na, K and Cs) materials were prepared, because it was known that the fully cation exchanged forms of this merlinoite undergo the transition below 1 bar CO_2.

Table 2. Window sizes within Li- and Li,M-MER structures. (dh), (h) and (ads) indicate dehydrated, hydrated and CO_2 loaded samples, respectively.

Sample	I (Å)	IIa (Å)	IIb (Å)	III (Å)
$Li_{6.2}$-MER (dh)	1.4(1)	1.3(1)	3.0(1)	1.1(1)
$Li_{6.2}$-MER (h)	3.7(1)	2.8(1)	3.5(1)	3.2(1)
$Li_{5.0}Na_{1.2}$-MER (dh)	1.4(1)	1.3(1)	3.0(1)	1.1(1)
$Li_{4.0}Na_{2.2}$-MER (dh)	1.6(1)	1.4(1)	3.1(1)	1.3(1)
$Li_{3.0}Na_{3.2}$-MER (dh)	1.6(1)	1.4(1)	3.0(1)	1.4(1)
$Li_{5.0}K_{1.2}$-MER (dh)	1.4(1)	1.4(1)	2.8(1)	1.2(1)
$Li_{4.0}K_{2.2}$-MER (dh)	1.5(1)	1.3(1)	3.1(1)	1.3(1)
$Li_{3.4}Cs_{2.8}$-MER (dh)	1.5(1)	1.1(1)	3.0(1)	1.6(1)
$Li_{3.4}Cs_{2.8}$-MER (h)	3.8(1)	3.0(1)	2.8(1)	3.2(1)
$Li_{3.4}Cs_{2.8}$-MER (ads)	3.9(1)	3.2(1)	3.0(1)	3.2(1)

PXRD patterns of these series of materials in their hydrated forms are given in Figure S1 in the SI. In each case single phase materials were prepared, and the compositional differences are evidenced by changes in the relative peak intensities. The PXRDs of dehydrated samples of the mixed cation series, by contrast, show additional reflections as the amount of the larger K and Cs cations is increased. This is observed for the $Li_{6.2-x}K_x$-series when $x > 2.2$ and for $Li_{6.2-x}Cs_x$ when $x > 2.8$ (Figures S2 and S3). For the Li,K-MER series these peaks may be attributed to K-poor and K-rich phases, *via* exsolution, as shown below. For the Li,Na-series (shown in Figure S1) there are no new resolved reflections but there is appreciable broadening of reflections for $x > 3.2$ that makes Rietveld refinement difficult. Rietveld analysis was therefore limited to those samples where a single *Immm* phase could be satisfactorily refined. Representative Rietveld plots of dehydrated $Li_{6.2}$-, $Li_{4.0}Na_{2.2}$-, $Li_{4.0}K_{2.2}$- and $Li_{3.4}Cs_{2.8}$-MER are shown in Figure 5 and representations of their structures are shown in Figure 6, with full refinement details listed in Table S2 and elsewhere in the SI. Figure 7 shows graphically the unit cell volumes of these and related phases.

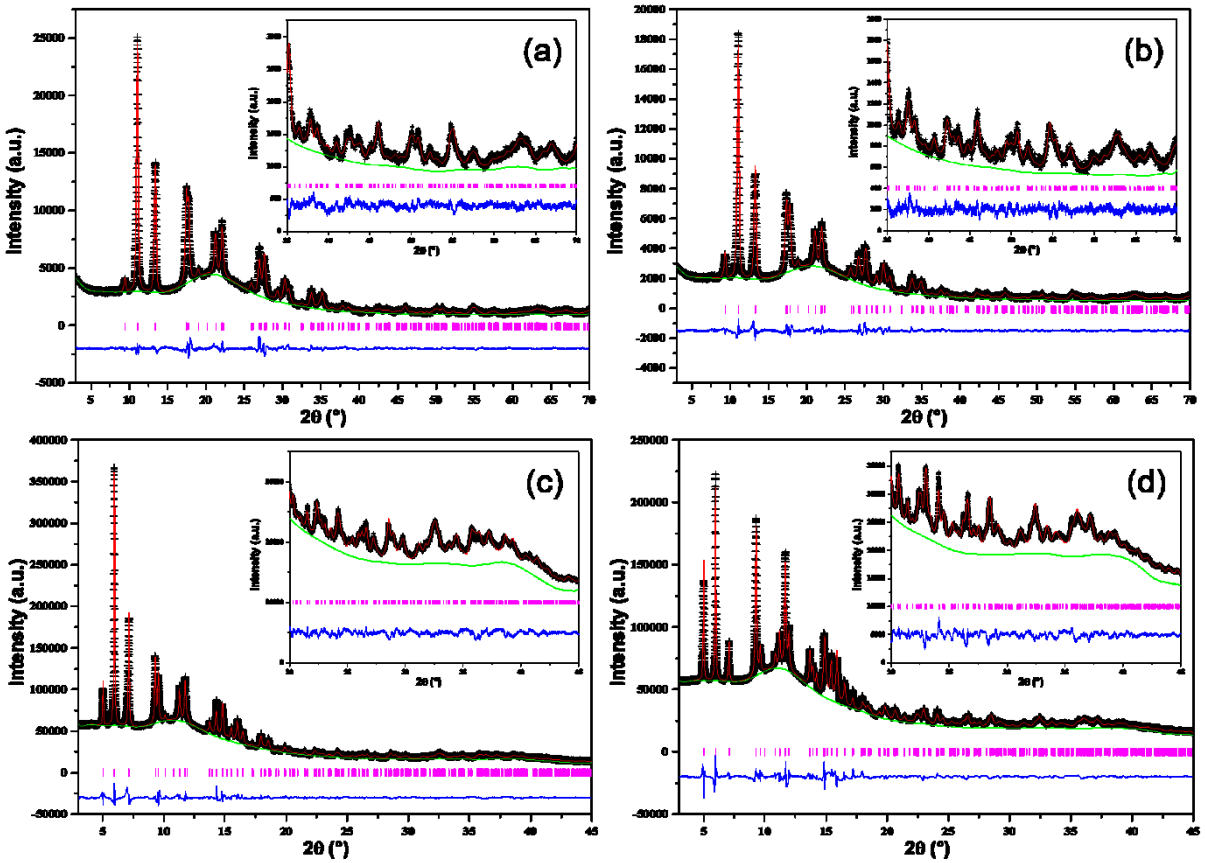

Figure 5. Rietveld plots of (a) $Li_{6.2}$-, (b) $Li_{4.0}Na_{2.2}$-, (c) $Li_{4.0}K_{2.2}$- and (d) $Li_{3.4}Cs_{2.8}$-MER, all dehydrated, with expansion of higher angle data shown inset. (λ = (a,b) 1.54056 Å, (c,d) 0.826398 Å).

Table 3. Site occupancies of M cations within Li- and Li,M-MER structures. (dh), (h) and (ads) indicate dehydrated, hydrated and CO_2 loaded samples, respectively. Frac and Abs denote fractional and absolute occupancies, respectively.

Sample	I			IIa			III		
	Frac	Ω	Abs	Frac	Ω	Abs	Frac	Ω	Abs
$Li_{4.0}Na_{2.2}$-MER (dh)	0.14(2)	4	0.6(1)	-			0.34(2)	4	1.4(1)
$Li_{3.0}Na_{3.2}$-MER (dh)	0.29(2)	4	1.2(1)	0.14(2)	4	0.6(1)	0.23(2)	4	0.9(1)
$Li_{5.0}K_{1.2}$-MER (dh)	-	-	-	-	-	-	0.17(1)	4	0.7(1)
$Li_{4.0}K_{2.2}$-MER (dh)	-	-	-	0.11(1)	4	0.4(1)	0.33(1)	4	1.3(1)
$Li_{3.4}Cs_{2.8}$-MER (dh)	0.08(1)	8	0.6(1)	-	-	-	0.91(1)	2	1.8(1)
$Li_{3.4}Cs_{2.8}$-MER (h)	0.35(1)	4	1.4(1)	0.28(1)	4	1.1(1)	0.30(1)	2	0.6(1)
$Li_{3.4}Cs_{2.8}$-MER (ads)	0.30(1)	4	1.2(1)	0.38(1)	4	1.5(1)	0.12(1)	2	0.2(1)

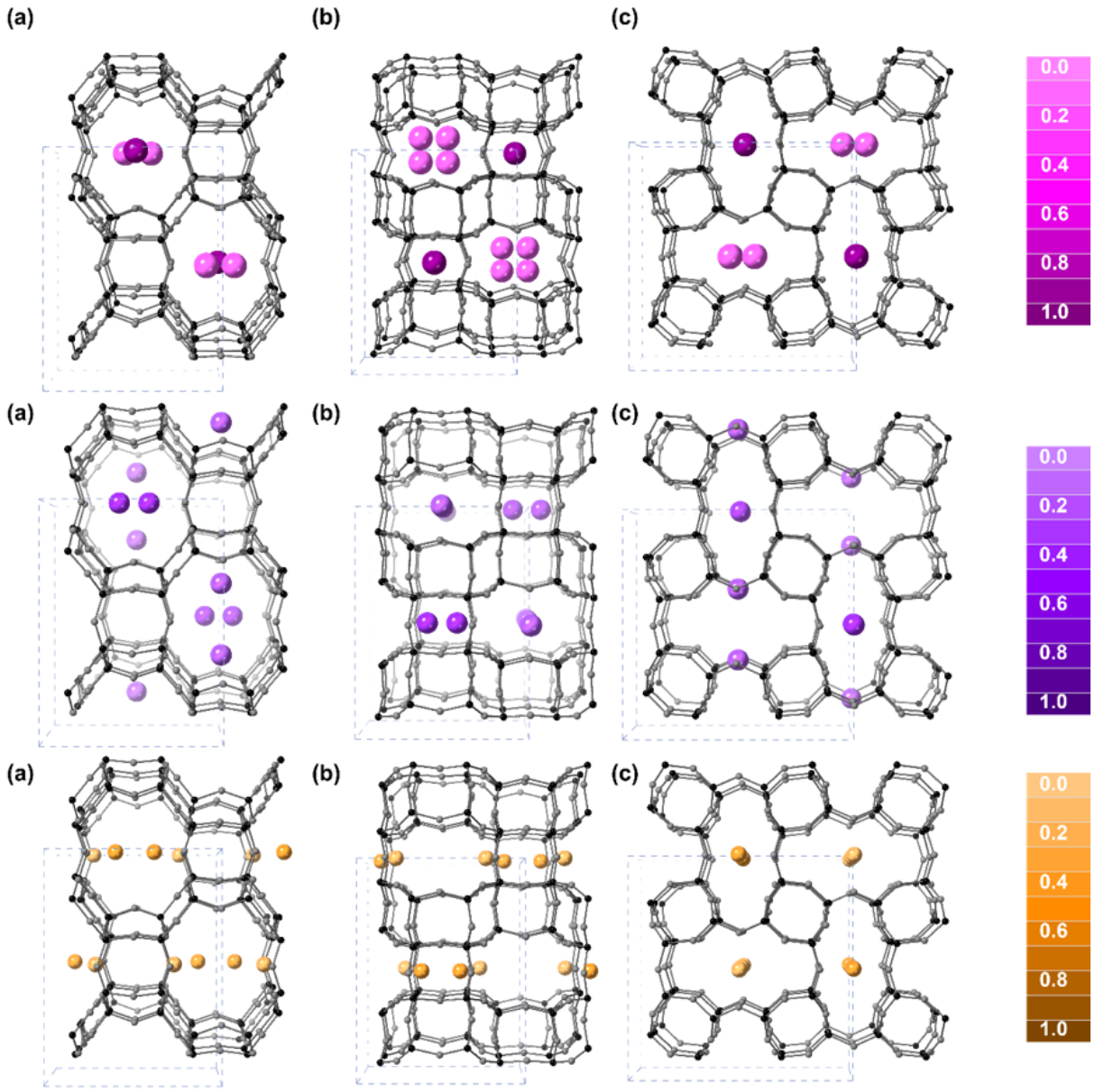

Figure 6. Extended structures of dehydrated forms of (bottom) $Li_{4.0}Na_{2.2}$-, (middle) $Li_{4.0}K_{2.2}$- and (top) $Li_{3.4}Cs_{2.8}$-MER as viewed down (a,b,c) a, b and c axes, respectively. T and O sites are shown in black and grey, with Na^+, K^+ and Cs^+ shown in shades of orange, purple and pink, respectively, with fractional occupancies described through shades indicated in legends on the right.

Fractional occupancies of cation sites are indicated by the intensities of the coloured cation representations in Figure 6 with more detailed information described in Table 3. As Li cations are extremely poor scatterers, their positions and occupancies could not be refined with any confidence. This was also the case for Na cations in $Li_{5.0}Na_{1.2}$-MER as the quantity of Na^+ was too low for unambiguous refinement.

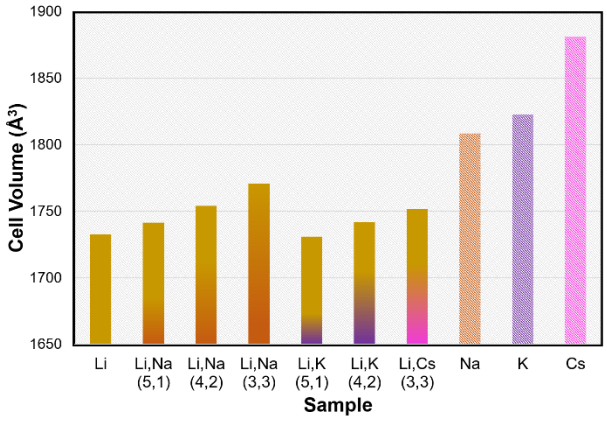

Figure 7. Unit cell volumes of MER materials. Cation form is shown below. Na-, K- and Cs-MER with Si/Al = 3.8 are shown for comparison.

In all dehydrated mixed cation materials, the larger cations preferentially occupied Site III, in the *ste* cavity. (Note that there are two *ste* cavities in the distorted *Immm* structure, only the larger of which is occupied by extra-framework cations in these structures.) Whereas the large Cs^+ occupies sites in the centre of the *ste* cavity, the smaller Na and K cations are displaced to 2 sites closer to the side of the cavity, with the displacement being greater for the Na cations. At higher levels of exchange, additional cations occupied sites within the *pau* cavity as well. From the neutron diffraction study of $Li_{6.2}$-MER, Li cations are known to favour S8R Site I, where they act to hold the framework in the contracted form, and it is likely that the Li cations in these mixed cation materials also predominantly occupy these narrow *d8r* sites and act to distort the dehydrated framework.

Figure 7 indicates that the unit cells of all Li-containing merlinoites are much smaller than those of their pure Na, K and Cs counterparts in MER(3.8), and the strong distortion of the frameworks, including the narrowing of the *d8r*s and single 8Rs, is illustrated in Figure 6, with quantification of window sizes in Table 2. Inclusion of the larger cations has relatively little effect because the *ste* cavity, even in the highly contracted Li-form, is sufficiently large to host even the largest Cs cation. Indeed, the smaller Na and K cations move off-centre in this cavity to achieve better coordination, as shown in Figure 6.

CO_2 Adsorption

The CO_2 sorption behaviour was investigated for those materials for which Rietveld refinement was possible using a single phase – all in the *Immm* space group. As mentioned earlier, Li-MER exhibits a lower uptake of CO_2 up to *ca.* 2.5 bar compared to previously investigated

MER materials, as shown in Figure 8, but exhibits uptake in excess of 5 mmol g^{-1} as the pressure is raised to 10 bar at 298 K (Figure S20). Based on previous observations for merlinoite, this second step to increased uptake is predicted to be due to a transition to a wide-pore structure.[23] Furthermore, the step is found to be temperature dependent, as expected, and the isotherms are reproduced after degassing by heating under vacuum.

The adsorption behaviour of the $Li_{6.2-x}Na_x$-MER series with $x \approx 1$, 2 and 3 is also shown in Figure 8 and Figure S21. The maximum uptake at 5 bar is ca. 5 mmol g^{-1}, and approaches that of the most porous of small pore zeolites LTA and RHO (ca. 6 mmol g^{-1}). Progressive introduction of Na^+ results in reduction of the pressure at which the isotherm step occurs, as well as less hysteresis in the desorption branch. This is an example of modifying zeolite adsorption behaviour through cation control. Similar behaviour is observed for the Li,K-MER series, shown in Figure 8, although this is complicated by exsolution as discussed below.

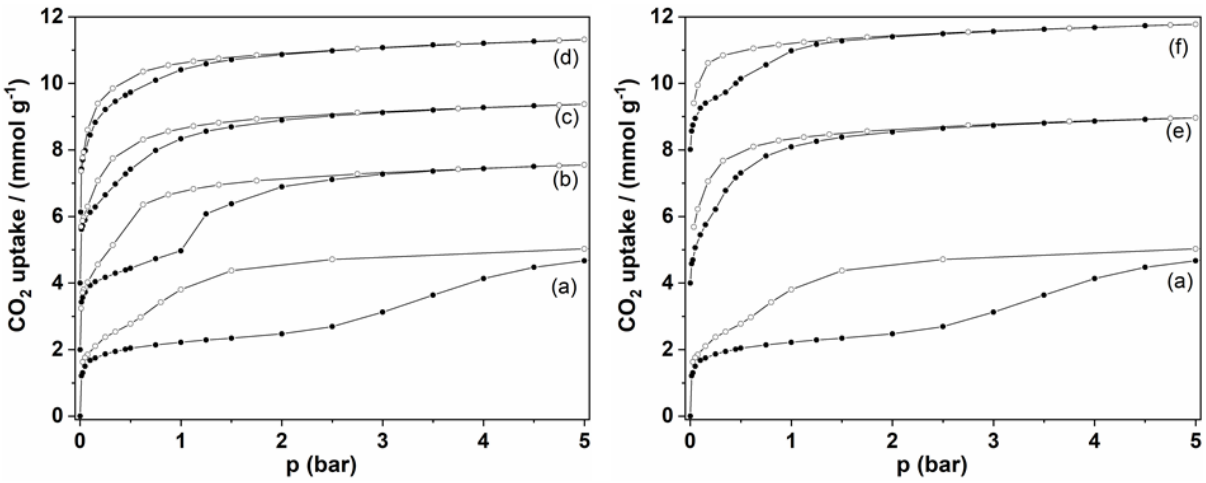

Figure 8. Stacked CO_2 sorption isotherms at 298 K up to 5 bar for Li,Na- and Li,K-MER, offset by (left) 2 and (right) 4 mmol g^{-1}, respectively: (a) $Li_{6.2}$-, (b) $Li_{5.0}Na_{1.2}$-, (c) $Li_{4.0}Na_{2.2}$-, (d) $Li_{3.0}Na_{3.2}$-, (e) $Li_{5.0}K_{1.2}$- and (f) $Li_{3.7}K_{2.5}$-MER. Adsorption and desorption curves are shown by open and closed circles, respectively. Note that $Li_{3.7}K_{2.5}$-MER (f) undergoes exsolution upon dehydration.

The effects on the CO_2 adsorption isotherm of adding larger alkali metal cations to Li-MER are compared in Figure 9 and Figures S21-S23. The uptake shown in Figure 9 is given in molecules per unit cell, because a gravimetric plot is influenced by the mass of the larger cations, particularly Cs^+ (Figure S24 gives the plots using mmol g^{-1}). $Li_{4.0}K_{2.2}$-MER exhibits behaviour similar to its Li,Na-MER analogue, showing a subtle kink in the adsorption isotherm at relatively low partial pressure, as well as greatly reduced hysteresis compared to the pure Li

material, whilst the Li,Cs-sample shows an adsorption step only at ~3 bar and major hysteresis between the adsorption and desorption branches.

In order to investigate the effect of cycling on the high pressure adsorption step observed for Li,Cs-MER, experiments were performed where the CO_2 pressure was cycled between 0 and 5 bar at 298 K, without heating during the evacuation to 0 bar. It can be seen from the adsorption/desorption cycles, shown in Figure 10, that with continued cycling a small but steadily increasing amount of CO_2 remained in the merlinoite after evacuation. This was accompanied by a progressive lowering in pressure at which the adsorption step occurred, due to structural transition to the wide-pore form of the material. As a result, the hysteresis gap closed and sorption behaviour became closer to that of $Li_{4.0}K_{2.2}$-MER. Finally, reactivation of the zeolite by extended evacuation and heating removes the bound CO_2 and again gives a step at elevated pressures of 2.5 bar and above as seen in Figure 10b.

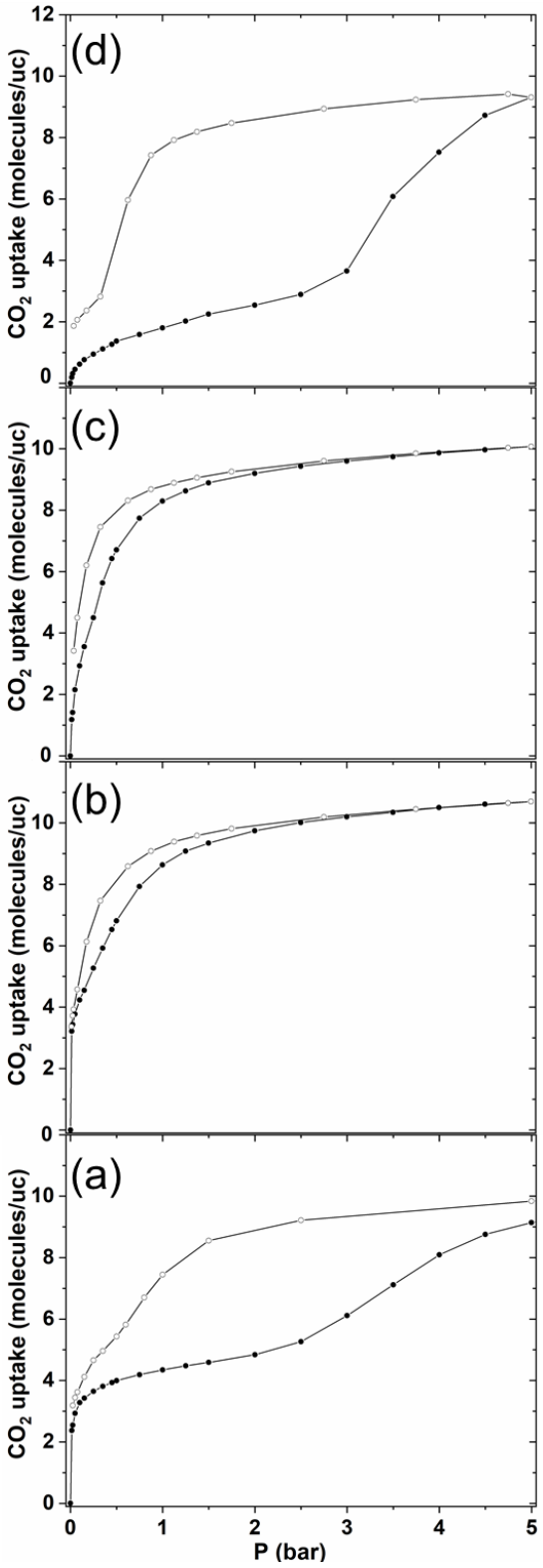

Figure 9. CO_2 adsorption isotherms at 298 K up to 5 bar for (a) $Li_{6.2}$-, (b) $Li_{4.0}Na_{2.2}$-, (c) $Li_{4.0}K_{2.2}$- and (d) $Li_{3.4}Cs_{2.8}$-MER. Adsorption, closed symbols; desorption, open symbols.

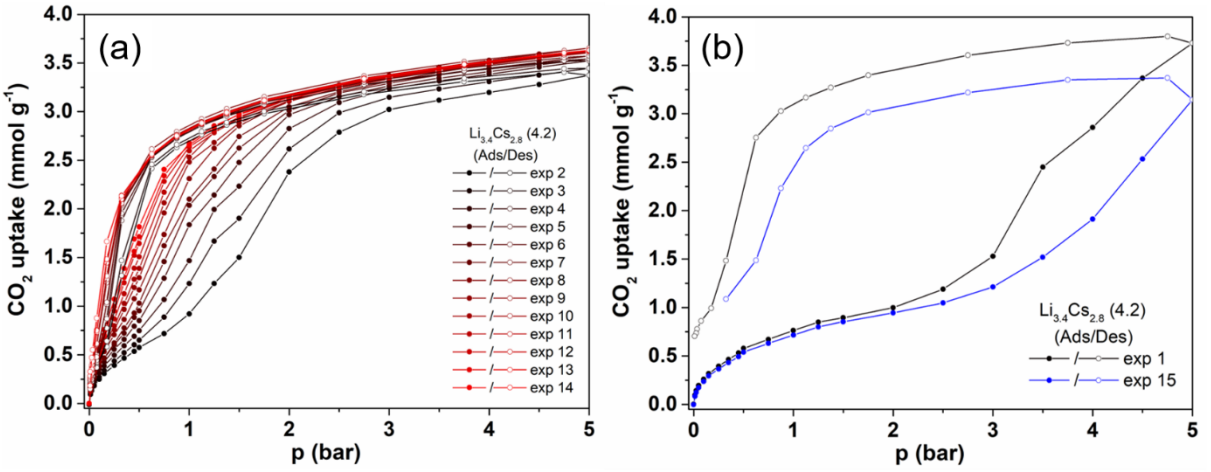

Figure 10. Cycling adsorption isotherms of Li,Cs-MER. (a) Isotherms collected after heating, before and after cyclical experiments (expts 1 and 15, respectively) and (b) consecutive adsorption isotherms collected with only evacuation between experiments.

Variable Pressure XRD experiments

Variable pressure PXRD (VPXRD) experiments using laboratory equipment allowed for extended investigation of the structural changes of $Li_{6.2}$-MER, $Li_{4.0}Na_{2.2}$-, $Li_{2.2}Na_4$- and $Li_{4.0}K_{2.2}$-MER upon adsorption of CO_2 at 298 K. Although pressures were limited to 1 bar and below on the apparatus used, this permitted observation of most of the important structural changes in the Li,Na- and Li,K-materials, whilst Li,Cs-MER was studied at beamline I11 at the Diamond Light Source, where operation under higher gas pressure was possible.

The limited quality of the data from the laboratory diffractometer does not allow detailed structural refinement but it was possible to identify phase changes. VPXRD patterns are shown in Figure 11, along with refined phase compositions, whilst the fits themselves are shown in Figure S14. The patterns were fitted with multiple phases where necessary, using dehydrated and hydrated Li-MER in structured fits for narrow- and wide-pore structures, respectively. This fitting showed that as well as narrow- and wide-pore phases observed previously, Li-containing MER structures exhibit an intermediate phase, behaviour that is similar to some compositions of the MOF, MIL-53.[27,48,49] This intermediate is present at low partial pressures of CO_2 in Li,Na-MER samples and only visible at very low CO_2 exposure for the Li,K-form. In Li-MER however, this intermediate phase is only observed at pressures close to 1 bar, whilst no wide-pore phase is observed over the pressure range investigated here.

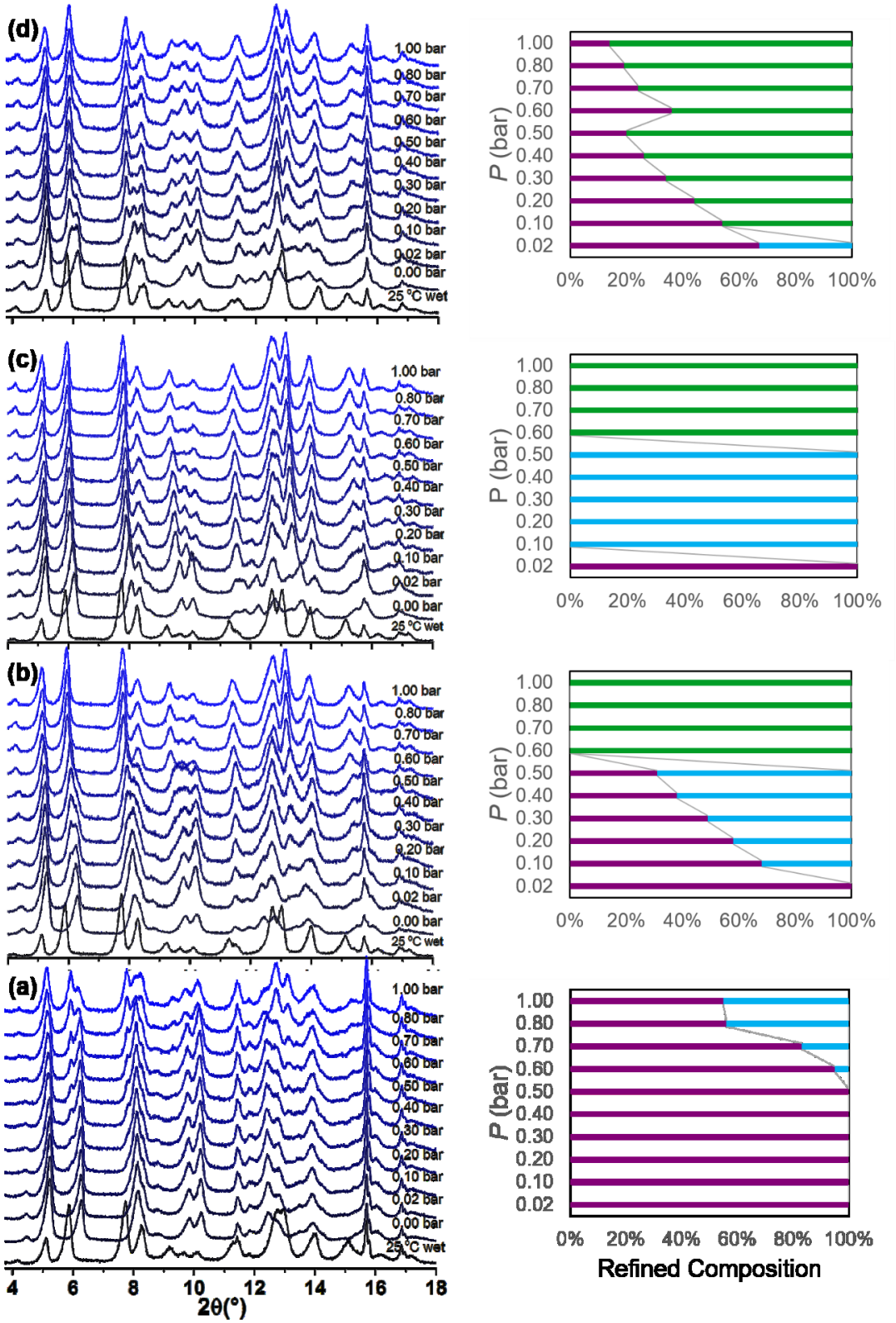

Figure 11. (Left) VPXRD experiments at 25 °C for (a) $Li_{6.2}$-, (b) $Li_{4.0}Na_{2.2}$-, (c) $Li_{2.0}Na_{4.2}$- and (d) $Li_{4.0}K_{2.2}$-MER. (Right) Relative fitted phase compositions of the 4 samples for each pressure. Narrow-, intermediate and wide-pore phases are indicated in purple, blue and green, respectively.

Structural Response to Adsorption in Li,Cs-MER

As stated, the narrow-to-wide pore transition could not be captured in the laboratory for $Li_{3,4}Cs_{2.8}$-MER because it takes place above 2 bar (see isotherm in Figure 9), but could be followed at beamline I11 at the Diamond Light Source synchrotron, where measurements were made up to 5 bar. Furthermore, this allowed for the collection of data of suitable quality for Rietveld refinement on the dehydrated material before and after adsorption of CO_2 at high pressure, as shown in Figure 12.

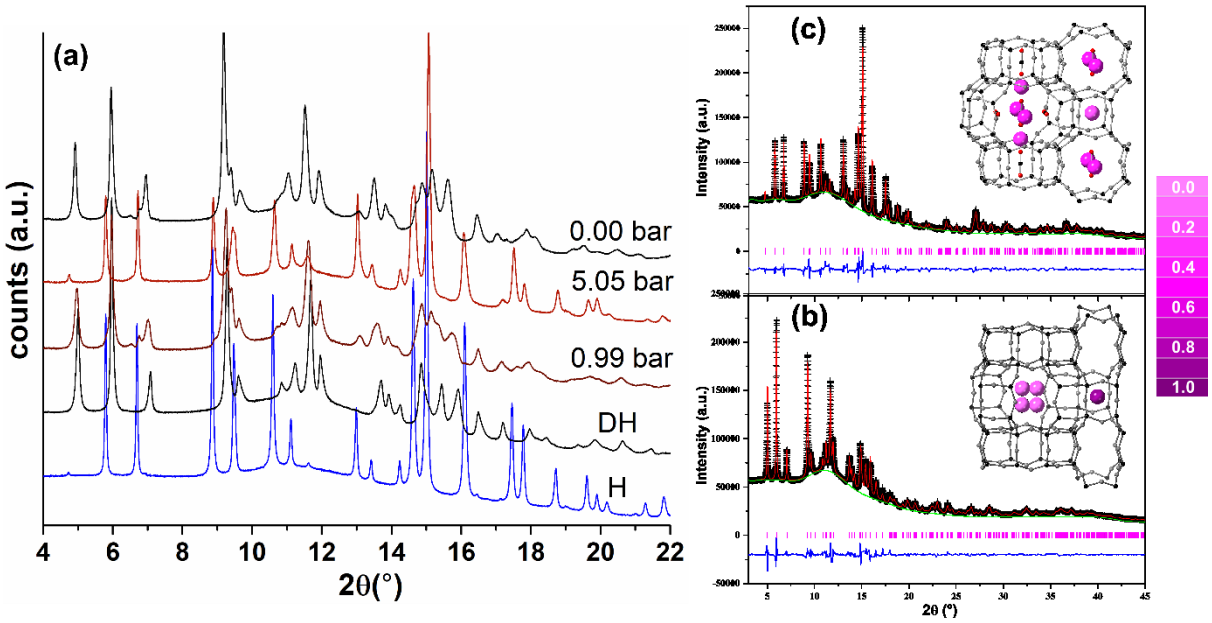

Figure 12 (a) Variable pressure synchrotron PXRD $Li_{3.4}Cs_{2.8}$-MER data with conditions indicated (H and DH correspond to hydrated and dehydrated, 0.00 bar indicates the evacuated sample after desorption) and Rietveld plots of (b) DH and (c) 5.05 bar data, with refined structures inset. T and O sites are shown in black and grey, with Cs^+ shown in shades of pink, with fractional occupancies described through shades indicated in the bar on the right. In the 5.05 bar structure, CO_2 is also shown as black and red molecules.

The structure of the dehydrated form was reported in Figure 6, where the Cs cations mainly occupy sites in the *ste* cavities with some in 8R sites of type I, although a little removed from the plane of these narrow 8Rs. The diffraction pattern at 980 mbar, corresponding to the lower uptake regime of the isotherm, is very similar to that of the dehydrated form, but with some additional reflections of low intensity. These did not occur at *d*-spacings observed at higher pressure for the wide-pore structure, suggesting an intermediate structure as a single phase with a slight change in symmetry. Full Rietveld refinement was not possible for this dataset.

At higher loadings, corresponding to the region above the kink in the isotherm when the uptake had reached ~3.5 mmol g^{-1}, a single phase was present, allowing for full structure refinement. The wide-pore, CO_2-bearing structure of Li,Cs-MER, and for comparison the dehydrated structure, are shown in Figures 12b and c, along with the Rietveld plots. At high pressure, the framework has expanded and the Cs cations in the preferred *ste* site of the dehydrated material had moved to occupy sites in 8Rs of the *pau* cavity, as quantified in Table 2.

Subsequent evacuation of the CO_2 gas at 298 K and measurement of the PXRD showed that the structure had reverted to a similar state to that observed at 980 mbar, which suggests that CO_2 encapsulation demonstrated in Figure 10 leads to structural similarities between the material after a sorption cycle and initial adsorption.

In summary, the presence of Li^+ in MER has important consequences for its structural and adsorptive behaviour. The modification of cation content can allow for tuning of adsorption behaviour, either through varying the cation type or the degree of exchange. The following Discussion attempts to synthesise and explain these results in terms of the flexibility of the MER framework and its response to the locations of cations and their migration upon CO_2 uptake. To aid in this, additional computational simulation and investigation of the time response of adsorption are taken into account.

Discussion

Li-MER possesses a highly contracted unit cell, resulting from the strong electrostatic forces the Li cations exert on the framework by virtue of their high charge density and the flexibility of the framework, which is able to distort strongly to provide narrow 8R sites. Li cations preferentially occupy the S8R sites in the extremely narrow *d8r* unit (Figure 4) which provides close coordination for them. Different modes of distortion are known for *d8r* units,[50] and comparison of those in Li-MER and Li-RHO are shown in Figures 13(e) and (f). In one case, the long axes of the elliptical 8Rs are parallel whilst in the other the long axes are perpendicular. Li^+ would not find good coordination to the more circular 8Rs found in less distorted MER frameworks (e.g. those adopted by all hydrated forms). The distortion causes *pau* cavities to form a set of narrow 8Rs at the expense of widening another set of 8Rs (the accessible 1D channel), as shown in Figure 13(a-d). The narrow and wide *ste* cavities, as mentioned earlier, are shown in Figures 13(a) and (b), with drastically different free window diameters of 1.3 and 3.0 Å, respectively.

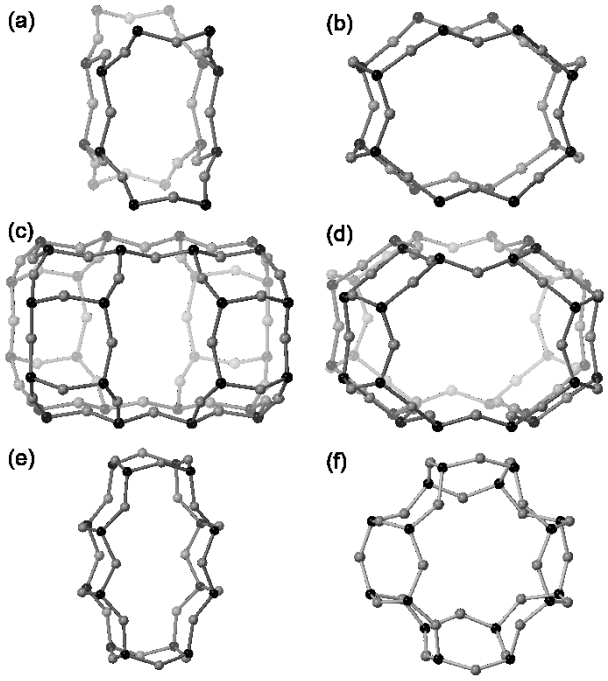

Figure 13. Cavities in dehydrated Li-MER:(a,b) narrow and wide ste cavities, (c,d) pau viewed down narrow and wide windows and (e) d8r. (f) d8r in dehydrated Li-RHO, for comparison.[8]

The distortion has important consequences for the dimensions of channels within the structure, with the free diameters of windows (calculated from the crystallographic O – O distances minus 2 times the van der Waals radius of O) listed in Table 2 for the series of refined structures.

Even though the effective diameter is larger than these values due to framework vibration (Cook and Connor suggest the window would act as if ~0.7 A larger),[51,52] the extremely narrow windows in the structure mean that percolation of CO_2 molecules is restricted to 1-dimensional channels, shown in solvent surface maps in Figure 14. Each dot corresponds to the centre of a solvent molecule passing over the framework surface, with connectivity between cavities showing that adsorbate diffusion is possible. Here a probe diameter of 2.3 Å was used as a reasonable representation of accessibility to CO_2 molecules taking into account an increase of 0.7 Å in the window size, above the crystallographic value, due to framework vibration.

This narrow-pore phase is shown by VPXRD to be adopted by Li-MER at 298 K until at least 1 bar of CO_2, when it is joined by a second, intermediate phase. This intermediate phase shows a slightly larger unit cell but does not resemble the fully open structure and has very little additional capacity. The observed Type I isotherm shape up to ~2 bar can then be explained by uptake in this 1D narrow pore system.

From 2.5 bar to 10 bar the uptake increases to ca. 5 mmol g^{-1} due to opening of the structure to the wide pore form. As described previously for other cation forms of MER(3.8),[23] this opening results when the gain in stability due to additional cation-CO_2 interactions in the wide pore form exceeds that due to the enhanced cation-framework interactions (Li-O in the distorted *d*8*r*s) in the narrow pore form.

Assuming the fully open Li-MER framework structure to resemble the framework structure of Li,Cs-MER in the fully open form (which has a very similar unit cell to hydrated Li-MER) and performing similar simulations, Figure 14 shows that CO_2 then gains three dimensional access to the pore space.

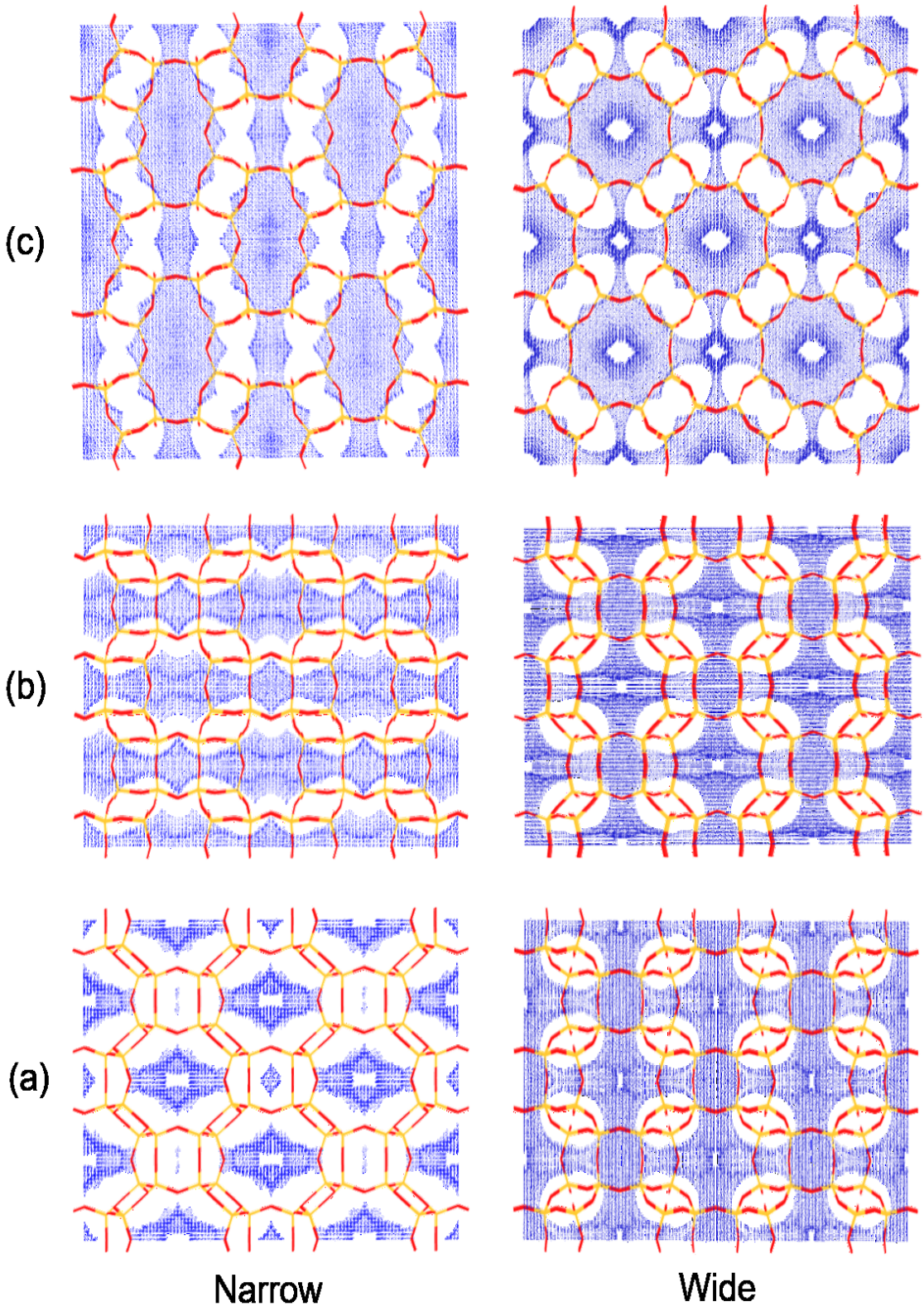

Figure 14. Solvent surfaces of the frameworks of (left) narrow- and (right) wide-pore Li-MER as viewed down the (a,b,c) x, y and z axes, respectively. The narrow pore framework has been determined experimentally, whereas the wide pore is taken as that of the hydrated form.

Calculated isotherms of narrow- and wide-pore silica frameworks, represented by those of the measured dehydrated $Li_{6.2}$-MER and the open Li,Cs-MER, with and without cations, are shown in Figure 15. These indicate that the pore space available upon transition to the open structure greatly increases. These are visualised for the pure silica narrow and wide pore structures at 5 bar in Figure S26. The presence of cations and charge in the simulation (solid lines) increases the uptake of CO_2 at lower fugacity but does not strongly affect the capacities at elevated fugacity. Values for the full narrow- and wide-pore structures of ~6 and ~11 molecules per unit cell, compare reasonably with experimental values of ~5 and 9 at 2.5 and 10 bar for Li-MER.

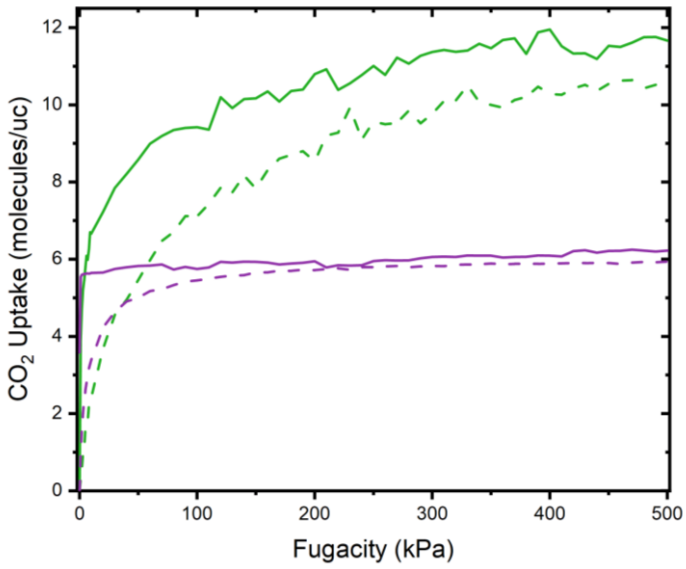

Figure 15. Calculated CO_2 adsorption isotherms of representative narrow and wide pore MER structures (Li-MER(dh) and Li,Cs-MER(CO_2)) in purple and green, respectively. Dashed and solid lines indicate pure silica and cation-containing model structures. The fugacity range of 0-500 kPa equates to ca. 0-5 bar.

Subsequently, we attempted to reduce the pressure at which the narrow-to-wide pore transition occurs by exchanging with larger cations. This was achieved to all levels, giving single phase hydrated materials with *Immm* symmetry. Upon activation of all these sorbents by dehydration, the presence of lithium results in strong contraction of the framework. However, rather than giving materials with similar unit cells that increase gradually with the incorporation of larger cations, as might have been expected from Vegard's Law, alternative types of behaviour are observed.

As Li^+ and Na^+ are both small cations, Na^+ sits relatively comfortably within the distorted MER structure. Indeed, Na-MER (3.8) adopted the *Immm* space group, as do samples here, whilst K and Cs analogues adopted $P4_2/nmc$. Therefore, at high Na^+ content minor symmetry changes may occur but site geometries are expected to remain favourable for both Li^+ and Na^+. In the Li,K-series, upon addition of K^+ above 2.2 per unit cell additional sets of peaks occur which can be explained by the presence of two *Immm* merlinoite phases, as explained below in terms of exsolution. Finally, for Li,Cs-MER with Cs^+ above 2.8, some additional peaks and peak splittings are observed, which are due to changes in unit cell size and symmetry, the details of which we have not yet been able to determine. These effects are thought to arise from competing demands on framework geometry from the large K and Cs and small Li cations.

As described above, Li^+ causes the framework to distort strongly, so that the majority of 8R window sites are not large enough for bulkier cations. However, the geometries of the *ste* sites are affected such that one is extremely wide, whilst the other is very narrow. This narrow *ste* cavity is not occupied by cations. Conversely, the wide *ste* cavity provides a favourable site for the added larger cations in dehydrated materials. Indeed, Cs^+ appears to fit snugly in the centre of this cavity, whilst the slightly smaller K^+ and Na^+ move progressively off-centre. Interestingly, previous work shows that the *ste* cavity is not the most favourable site in pure Na- and K-materials and therefore site occupancies are affected by Li cations distorting the structure, or competition with Li^+ for more favourable sites.[23]

When the number of larger cations is greater than 2 (the multiplicity of the larger *ste* cavities in *Immm*), sites other than the *ste* cavity must be found, so that structural change is required in the dehydrated form. For Na^+, the cation size is sufficiently similar to Li^+ for the adaptation to be slight, manifesting as intracrystalline strain and peak broadening, while for $Li_{6.2-x}K_x$-MER with $x > 2.2$, the materials respond by exsolution. This is seen in $Li_{3.7}K_{2.5}$-MER, the PXRD pattern of which is shown in Figure S14. Here exsolution occurs, with 2 phases showing drastically different unit cell volumes of 1753.9 and 1953.3 $Å^3$, the smaller possessing lower K^+ content, with cations sitting predominantly in Site III, the wide *ste* cavity. The larger phase, by contrast, appears to be a pure K-MER phase and its unit cell volume is very similar to those observed in wide-pore phases, such as hydrated Li-MER. The cation siting here is unlike other samples investigated and is indeed more like K-MER(3.8). This reflects the expanded unit cell and subsequent alteration of site preferences, the driving force for exsolution to occur. Further details can be found in the SI (Tables S3, S14, S15). Exsolution has been described relatively rarely in zeolites: Pakhomova *et al*. describe the exsolution of Na- and K- in Na,K-amicite

(GIS) – another zeolite with a flexible structure that shows significant framework contraction when dehydrated - and adopts Na- and K-forms with strongly different unit cell volumes.[53]

The presence of ~2 larger cations in the dehydrated forms of single phase Li,M-merlinoites has relatively little effect on the framework geometry due to the provision of suitable locations in the spacious *ste* sites. The narrow-pore forms of these materials have similar 1D pore geometries to the pure Li-MER. Nevertheless, the presence of the larger cations strongly affects the CO_2 adsorption properties, either in isotherm shape or uptake kinetics. Li,Na-MER and Li,K-MER have strongly reduced narrow-to-wide pore transition pressures (the correlation of the increased uptake and the appearance of the wide pore phase is shown unambiguously by comparison of the isotherms and the VPXRD measurements). By contrast, Li,Cs-MER has a similarly high transition pressure to Li-MER (3 bar), but shows much slower adsorption.

CO_2 Adsorption on Li,Na- and Li,K-MER

For both the Li,Na- and Li,K-MER materials, the presence of even one larger cation per unit cell has a strong effect in lowering the opening pressure. This is increased by further addition, so that for contents of around 2 Na or K cations per unit cell, the transition to the wide form is complete or almost complete by 1 bar. This effect is seen clearly for the Li,Na-series, but also for the Li,K-analogues, where inclusion of 1.2 K^+ gives an inflection point at ~2.5 mmol g^{-1}, as shown in Figure S22).

The incorporation of either Na^+ or K^+ increases the unit cell size steadily, as shown in Figure 7. Notably, Na^+ materials possess larger unit cell volumes than their respective K^+ analogues, suggesting higher occupation of Site I seen for the Li,Na-MER series has a greater effect on framework geometry and unit cell volume than K^+ occupation of Site IIa. In both series, as more Na or K cations are added to the material, the energies of the narrow- and wide-pore materials become more similar (these cations provide less stabilisation than Li^+ for the contracted form) and hence expansion occurs at a lower partial pressure.

While this helps to describe the effect of Na and K cations on the initial narrow-pore and the fully open structures on the resulting adsorption isotherms, *in situ* VPXRD experiments have revealed an additional complexity – the presence of an intermediate phase between narrow and wide pore materials as pressure is increased during the adsorption. VPXRD data of $Li_{2.0}Na_{4.2}$-MER consists of a pure intermediate phase between 100 and 500 mbar, and Rietveld refinement gives a low resolution structure that indicates narrow windows, as detailed in Table S16. Whilst the detailed structure of the intermediates in these experiments awaits more detailed

investigation, it is clear that the flexibility of the MER framework allows it many alternative modes of distortion to minimise its total energy upon adsorption. The limited effect of the intermediate on adsorption uptake is highlighted by comparison of $Li_{4.0}Na_{2.2}$- and $Li_{2.0}Na_{4.2}$-samples. Whilst $Li_{2.0}Na_{4.2}$-MER shows an isolated intermediate structure at a range of pressures, the $Li_{4.0}Na_{2.2}$-sample exhibits gradual conversion of the narrow-pore to the intermediate structure. Despite this, examination of their respective isotherms shows a step at very similar pCO_2, corresponding to the transition to the wide-pore structure.

The nature of structural transitions in the materials investigated were not identical. In Li,K-MER, the narrow- and wide-pore forms are observed simultaneously, whilst for Li,Na-MER the intermediate is seen at increasingly high quantities until a threshold partial pressure, at which point only the wide-pore form is seen. This suggests that the transition from the intermediate to the wide-pore form is more readily achieved than the transition from the narrow-pore form to the intermediate. Together with the presence of a kink in the isotherm, this suggests that cooperative effects may be present, as once an intermediate structure changes to the wide-pore form in a local region, it is more favourable for adjacent regions to undergo the same transition. As further evidence for this, it should be noted that the intermediate and wide-pore forms are not observed concurrently.

The slight increase in unit cell volume with the intermediate structures in these transitions may allow for an easier transition to the wide-pore structure than from the extremely distorted dehydrated material. The different behaviour of the cation forms also suggests that the transitions may be modulated by cation type and hence may be impacted by cation siting or mobility. This could be in line with the work of Balesta *et al.*, which suggested that inhibited cation hopping led to the presence of long-lived metastable structures due to the trapping of cations in crystallographic sites.[54]

CO_2 Adsorption on Li,Cs-MER

In contrast to Na^+ and K^+, the presence of 2.8 Cs^+ per unit cell does not reduce the transition pressure, but instead this material opens above ca. 3 bar, similar to Li-MER. We speculate that this is due to favourable siting of Cs^+ within the *ste* cavity. In pure Cs-MER(3.8), Site III was the most favoured and it is likely that the presence of Cs^+ in this *ste* cage stabilises the narrow-pore structure in $Li_{3.4}Cs_{2.8}$-MER similarly to Li^+ and more than either Na^+ or K^+.

As a consequence of this higher transition pressure and the resulting well defined regions where the $Li_{3.4}Cs_{2.8}$-MER is in narrow and wide pore forms, it is possible to obtain high resolution

structures in narrow (dehydrated) and wide pore (5 bar CO_2) forms. The Cs cations have dispersed from their favoured *ste* locations in the narrow pore to 8R sites in the open structure. Given these framework structures, it is possible to examine likely pore connectivity and uptakes in the two forms, which gives results similar to those shown for narrow and wide pore Li-MER structures (Figures 14 and 15).

Examination of experimental and calculated isotherms in Figures 10, 15 and S25 show that it is possible to observe a major increase in uptake (>100% in the modelling) with only a relatively small increase in the unit cell size. In this way the breathing mode of merlinoite differs substantially from that observed in MIL-53, where the whole unit cell shows a major expansion. A general model is shown schematically in Figure 16. At a critical uptake of CO_2, the narrow-pore structure undergoes transition to the wide-pore form, greatly increasing pore volume as well as channel connectivity. Hysteresis is observed for many of these materials.

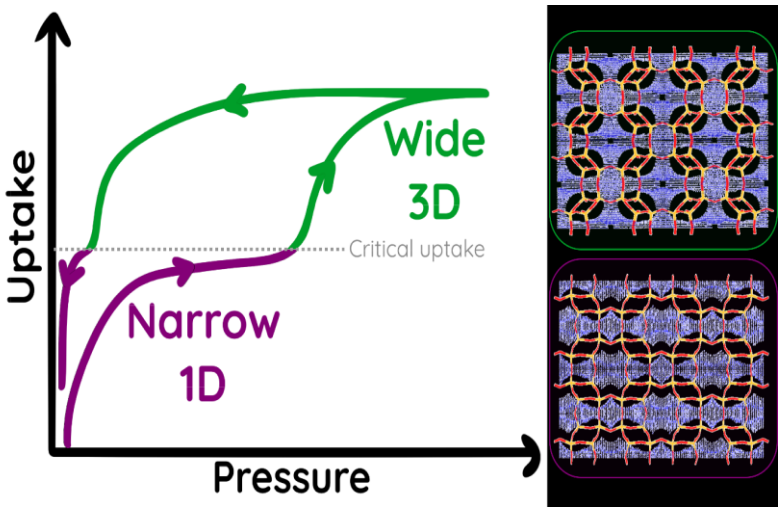

Figure 16. Schematic isotherm of Li,M-MER materials. Below critical uptake, the narrow MER structure with 1D channels is adopted and above which a wide-pore stucture with 3D connectivity is found. Such structures and their connectivity are shown on the right, in the form of solvent surfaces viewed down the y axis.

Comparison of the isotherms in Figure 9 also suggest that lower uptake occurs in $Li_{3.4}Cs_{2.8}$-MER than in $Li_{6.2}$-MER up to ~2.5 bar of CO_2. In Li,Cs-MER uptake into the 1-D channel system is hindered by the presence of cations in the *ste* cavity. Whilst this is likely to be the case in other materials, in this sample Site III is almost fully occupied by Cs^+, the largest of the cations investigated here, as shown in Figure 12. Percolation through the materials in the narrow-pore phase must therefore require cation gating. A scheme depicting percolation through $Li_{3.4}Cs_{2.8}$-MER is shown in Figure 17, with a large Cs cation initially blocking percolation through the *ste* site. Only once Cs^+ moves from this favourable site can CO_2 pass through the cavity, which may occur through interaction with CO_2 molecules drawing the cation from one site to a neighbouring site in the *pau* cavity. This may be facilitated by movement of other cations or by the presence of empty neighbouring sites, as suggested by Mace *et al*.[55] Once moved to the adjacent *pau* site, the Cs cation may return to the *ste* site assisted by CO_2 molecules or through thermal motion. A threshold CO_2 uptake may be required to ease Cs^+ displacement, as Shang *et al.* have shown that the barrier to cation movement in Cs-CHA is reduced as the number of CO_2 molecules increases.[29] Alternatively, this might be explained by thermal motion of the cation, as proposed by Coudert and Kohen.[56]

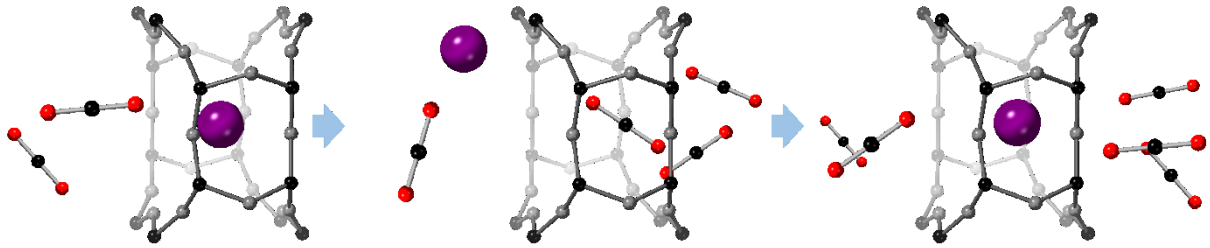

Figure 17. A potential mechanism of percolation through Li,Cs-MER. A Cs cation moves from the ste site to a vacant site in the pau cavity, aided by interaction with a CO_2 molecule. The cation may return to the ste site assisted by CO_2 or through thermal motion. Framework atoms are shown as black and grey for T and O sites, respectively. Cs^+ is shown in purple, whilst CO_2 molecules are black and red.

This behaviour has substantial effects on adsorption kinetics. Whilst adsorption isotherms are ideally measured under thermodynamic control, examination of the time dependent uptake data, shown in Figure 18, suggests that some of these materials possess slow kinetics of adsorption, with $Li_{3.4}Cs_{2.8}$-MER particularly slow. From the individual adsorption steps (inset), and for $Li_{3.4}Cs_{2.8}$-MER especially, uptake is slow to reach equilibrium. Conversely, the Li-form appears to undergo a sharp uptake at the beginning of the dosing step followed by a flatter, though still non-asymptotic, curve. As a result, the uptake of the $Li_{3.4}Cs_{2.8}$- and $Li_{6.2}$-MER materials cannot be readily compared at low partial pressure. The addition of Cs cations has

slowed percolation through the material to the extent that truly equilibrated measurements would be prohibitively long. Reduced Cs^+ content and hence lower occupancy of the vital *ste* cavity may allow for precise control of sorption kinetics and be of interest in kinetic separation technologies.

It is interesting to note that Li-MER appears to show the fastest adsorption kinetics of the samples investigated based on the curves shown in Figure 18 and yet does not open to the wide-pore form below 2.5 bar. This provides further evidence that the step in Li-MER adsorption is a thermodynamic, rather than a kinetic consideration. However, this is complicated in Li,Cs-MER, by kinetically-limited initial adsorption.

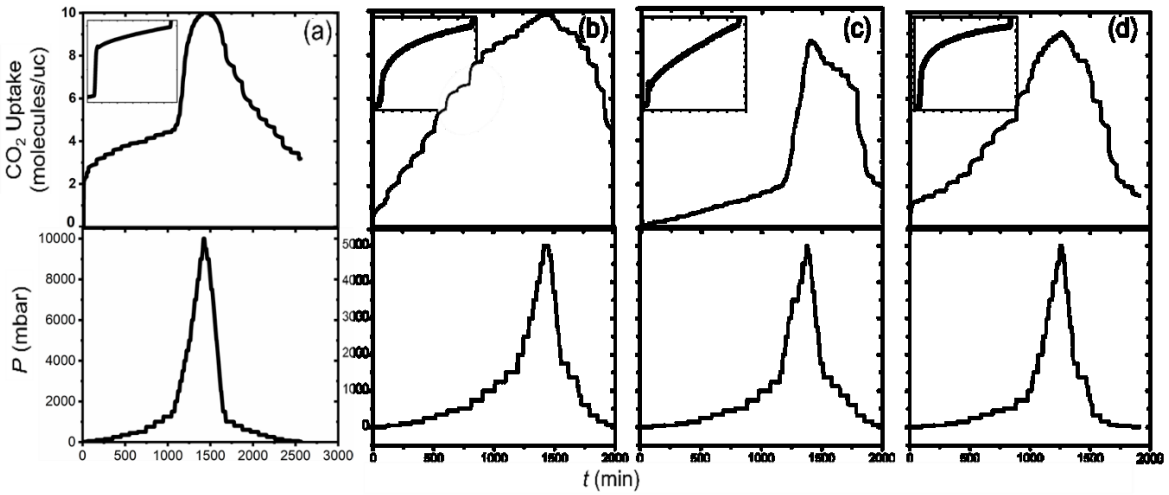

Figure 18. (a,b,c) CO_2 uptake at 298 K over the course of adsorption experiments with relevant dosing pressure steps shown below for $Li_{6.2}$-, $Li_{4.0}K_{2.2}$- and $Li_{3.4}Cs_{2.8}$-MER. P_{CO2} up to 5 bar in (b) and (c), but 10 bar for (a). (d,) Corresponding plots for $Li_{3.4}Cs_{2.8}$-MER after consecutive adsorption experiments without thermal activation. Individual adsorption steps for a given low pressure dose are inset.

Comparison of $Li_{3.4}Cs_{2.8}$-MER after activation and non-activated sorption cycles shown in Figure 18(c) and (d), respectively, show strongly different kinetics. The sample containing residual CO_2 shows improved kinetic behaviour, consistent with the greater uptake at a given pressure observed in Figure 10. This is of interest for potential application, because while the freshly activated material shows poor sorption kinetics, subsequent cycles may allow for access to the full working capacity over a narrower pressure range, accompanied by faster diffusion of CO_2. The residual CO_2 that is observed as a result of cycling may be indicative of chemisorption occurring. Such behaviour and formation of carbonate species has been reported

in small pore zeolites including ZK-5 and zeolite A.[57,58] It may be that this is facilitated by small amounts of residual water in the zeolites or in the added CO_2. In any case, the presence of CO_2 retained in the structure after evacuation makes transition to the wide pore form possible at lower p_{CO2}.

Conclusion

Fully-exchanged Li-MER has been prepared for the first time. In the dehydrated state this has a strongly distorted framework with very narrow d8r units and a reduced unit cell volume. Neutron diffraction indicates that the preferred sites for the Li cations are the S8R sites in these d8r units and it is likely the distortion results to enable their favourable coordination.

Li-MER(4.2) exhibits interesting step-like adsorption behaviour for CO_2 and that this behaviour may be modified through the introduction of a second, larger, alkali metal cation. Narrow-pore versions of these materials adopted upon dehydration exhibit a high degree of distortion, sometimes leading to exsolution effects. In the narrow-pore dehydrated materials that are single phase, analysis of the framework distortion shows that it leads to a reduction in channel connectivity for CO_2 adsorbate from three dimensions to one, hindering percolation of CO_2 through the material. This is exacerbated in Li,Cs-MER by the presence of large Cs cations in vital *ste* cavities, resulting in exceptionally slow adsorption kinetics.

Transitions from narrow- to wide-pore forms of zeolite MER result in important increases of uptake of CO_2, as more of the pore space becomes accessible, giving uptakes at 298 K of *ca.* 5 mmol g^{-1}. These steps in uptake occur at lower partial pressures in Li,Na- and Li,K-MER compared to Li-MER and proceed *via* intermediate structures.

There is considerable hysteresis in the desorption branch, which leads to 'encapsulation' of CO_2 down to low pressure, but in repeated adsorption/desorption cycles without heating after desorption to 0 bar, residual CO_2 within the material after repeated adsorption cycles greatly improves sorption kinetics and further alters the step-like adsorption behaviour.

Supporting Information

Supporting Information is available free of charge on the ACS Publications website at [doi**********] including details of ICP analysis of lithium content, powder X-ray and neutron diffraction and crystallographic analysis (including cif files) on hydrated and

dehydrated merlinoites, computer simulation of lithium siting in merlinoite and of CO_2 adsorption isotherms, experimental CO_2 adsorption isotherms and TGA (PDF).

Acknowledgements

The authors thank the EPSRC for funding (Cation-Controlled Gating for Selective Gas Adsorption over Adaptable Zeolites: EP/N032942/1, V.M.G., P.A.W. and an NPIF Ph.D. scholarship for E.L.B.: EP/R512199/1). We acknowledge Diamond Light Source for time on Beamline I11 under Proposal CY22322-1. Experiments at the ISIS Neutron and Muon Source were supported by a beamtime allocation RB2090052-1 from the Science and Technology Facilities Council. Drs. Yuri Andreev and Julia L. Payne (University of St. Andrews) are thanked for assistance with *in situ* PXRD and sample preparation, respectively. Prof. Paul A. Cox (Portsmouth University) is thanked for helpful suggestions. The raw data accompanying this publication are directly available at https://doi.org/10.17630/cac904b4-3c07-4159-913f-80ff53b13bb7 [reference 59] and, for the neutron powder diffraction data, https://doi.org/10.5286/ISIS.E.RB2090052-1

References

(1) Moliner, M.; Martínez, C.; Corma, A.; Mart, C.; Corma, A. Synthesis Strategies for Preparing Useful Small Pore Zeolites and Zeotypes for Gas Separations and Catalysis. *Chem. Mater.* **2014**, *26*, 246–258.

(2) Zanota, M. L.; Heymans, N.; Gilles, F.; Su, B. L.; De Weireld, G. Thermodynamic Study of LiNaK-LSX Zeolites with Different Li Exchange Rate for N_2/O_2 Separation Process. *Microporous Mesoporous Mater*. **2011**, *143*, 302–310.

(3) Delgado, J. A.; Águeda, V. I.; Uguina, M. A.; Sotelo, J. L.; Brea, P.; Grande, C. A. Adsorption and Diffusion of H_2, CO, CH_4, and CO_2 in BPL Activated Carbon and 13X Zeolite: Evaluation of Performance in Pressure Swing Adsorption Hydrogen Purification by Simulation. *Ind. Eng. Chem. Res.* **2014**, *53*, 15414–15426.

(4) Shang, J.; Hanif, A.; Li, G.; Xiao, G.; Liu, J. Z.; Xiao, P.; Webley, P. A. Separation of CO_2 and CH_4 by Pressure Swing Adsorption Using a Molecular Trapdoor Chabazite Adsorbent for Natural Gas Purification. *Ind. Eng. Chem. Res*. **2020**, *59*, 7857-7865.

(5) Welk, M. E.; Nenoff, T. M.; Bonhomme, F. Defect-Free Zeolite Thin Film Membranes for H_2 Purification and CO_2 Separation. In Studies in Surface Science and Catalysis; van Steen, E., Callanan, L. H., Claeys, M., Eds.; Elsevier B.V.: Cape Town, South Africa, **2004**; Vol. 154 A, pp 690–694.

(6) Palomino, M.; Corma, A.; Rey, F.; Valencia, S. New Insights on CO_2-Methane Separation Using LTA Zeolites with Different Si/Al Ratios and a First Comparison with MOFs. *Langmuir* **2010**, *26*, 1910–1917.

(7) Ridha, F. N.; Webley, P. A. Anomalous Henry's Law Behavior of Nitrogen and Carbon Dioxide Adsorption on Alkali-Exchanged Chabazite Zeolites. *Sep. Purif. Technol*. **2009**, *67*, 336–343.

(8) Łozińska, M. M.; Mangano, E.; Greenaway, A. G.; Fletcher, R.; Thompson, S. P.; Murray, C. A.; Brandani, S.; Wright, P. A. Cation Control of Molecular Sieving by Flexible Li-Containing Zeolite Rho. *J. Phys. Chem. C* **2016**, *120*, 19652–19662.

(9) Palomino, M.; Corma, A.; Jordà, J. L.; Rey, F.; Valencia, S. Zeolite Rho: A Highly Selective Adsorbent for CO_2/CH_4 Separation Induced by a Structural Phase Modification. *Chem. Commun*. **2012**, *48*, 215–217.

(10) Du, T.; Fang, X.; Liu, L.; Shang, J.; Zhang, B.; Wei, Y.; Gong, H.; Rahman, S.; May, E. F.; Webley, P. A.; Li, G. An Optimal Trapdoor Zeolite for Exclusive Admission of CO_2 at Industrial Carbon Capture Operating Temperatures. *Chem. Commun*. **2018**, *54*, 3134–3137.

(11) Liu, Q.; Mace, A.; Bacsik, Z.; Sun, J.; Laaksonen, A.; Hedin, N. NaKA Sorbents with High CO_2-over-N_2 Selectivity and High Capacity to Adsorb CO_2. *Chem. Commun*. **2010**, *46*, 4502–4504.

(12) IZA Database of Zeolite Structures http://europe.iza-structure.org (accessed Sep 1, 2020).

(13) Thang, H. V.; Grajciar, L.; Nachtigall, P.; Bludský, O.; Areán, C. O.; Frýdová, E.; Bulánek, R. Adsorption of CO_2 in FAU Zeolites: Effect of Zeolite Composition. *Catal. Today* **2014**, *227*, 50–56.

(14) Maurin, G.; Belmabkhout, Y.; Pirngruber, G.; Gaberova, L.; Llewellyn, P. CO_2 Adsorption in LiY and NaY at High Temperature: Molecular Simulations Compared to

Experiments. *Adsorption* **2007**, *13*, 453–460.

(15) Yasuhisa, H.; Watanabe, K.; Kusakabe, K.; Morooka, S. The Separation of CO_2 Using Y-Type Zeolite Membranes Ion-Exchanged with Alkali Metal Cations. *Sep. Purif. Technol*. **2001**, *22–23*, 319–325.

(16) Grajciar, L.; Čejka, J.; Zukal, A.; Otero Areán, C.; Turnes Palomino, G.; Nachtigall, P. Controlling the Adsorption Enthalpy of CO_2 in Zeolites by Framework Topology and Composition. *ChemSusChem* **2012**, *5*, 2011–2022.

(17) Llewellyn, P. L.; Maurin, G. Gas Adsorption Microcalorimetry and Modelling to Characterise Zeolites and Related Materials. *Comptes Rendus Chim*. **2005**, *8*, 283–302.

(18) Plant, D. F.; Maurin, G.; Deroche, I.; Gaberova, L.; Llewellyn, P. L. CO_2 Adsorption in Alkali Cation Exchanged Y Faujasites: A Quantum Chemical Study Compared to Experiments. *Chem. Phys. Lett*. **2006**, *426*, 387–392.

(19) Smith, L. J.; Eckert, H.; Cheetham, A. K. Site Preferences in the Mixed Cation Zeolite, Li,Na-Chabazite: A Combined Solid-State NMR and Neutron Diffraction Study. *J. Am. Chem. Soc.* **2000**, *122*, 1700–1708.

(20) Baksh, M. S. A.; Kikkinides, E. S.; Yang, R. T. Lithium Type X Zeolite as a Superior Sorbent for Air Separation. *Sep. Sci. Technol*. **1992**, *27*, 277–294.

(21) Gaffney, T. R. Porous Solids for Air Separation. *Curr. Opin. Solid State Mater. Sci.* **1996**, *1*, 69–75.

(22) Feuerstein, M.; Engelhardt, G.; McDaniel, P. L.; MacDougall, J. E.; Gaffney, T. R. Solid-State Nuclear Magnetic Resonance Investigation of Cation Siting in LiNaLSX Zeolites. *Microporous Mesoporous Mater*. **1998**, *26*, 27–35.

(23) Georgieva, V. M.; Bruce, E. L.; Verbraeken, M. C.; Scott, A. R.; Casteel, W. J.; Brandani, S.; Wright, P. A. Triggered Gate Opening and Breathing Effects during Selective CO_2 Adsorption by Merlinoite Zeolite. *J. Am. Chem. Soc.* **2019**, *141*, 12744–12759.

(24) Choi, H. J.; Min, J. G.; Ahn, S. H.; Shin, J.; Hong, S. B.; Radhakrishnan, S.; Chandran, C. V.; Bell, R. G.; Breynaert, E.; Kirschhock, C. E. A. Framework Flexibility-Driven CO_2 Adsorption on a Zeolite. *Mater. Horizons* **2020**, *7*, 1528−1532.

(25) Choi, H.J.; Jo, D.; Min, J. G.; Hong, S. B., The Origin of Selective Adsorption of CO_2 on Merlinoite Zeolites. *Angew. Chem. Int. Ed*. **2020**, *59*, 2-10.

(26) Shang, J.; Li, G.; Singh, R.; Gu, Q.; Nairn, K. M.; Bastow, T. J.; Medhekar, N.; Doherty, C. M.; Hill, A. J.; Liu, J. Z.; Webley, P. A. Discriminative Separation of Gases by a "Molecular Trapdoor" Mechanism in Chabazite Zeolites. *J. Am. Chem. Soc.* **2012**, *134*, 19246–19253.

(27) Kondo, A.; Yashiro, T.; Okada, N.; Hiraide, S.; Ohkubo, T.; Tanaka, H.; Maeda, K. Selective Molecular-Gating Adsorption in a Novel Copper-Based Metal-Organic Framework. *J. Mater. Chem. A* **2018**, *6*, 5910–5918.

(28) Chen, L.; Mowat, J. P. S.; Fairen-Jimenez, D.; Morrison, C. A.; Thompson, S. P.; Wright, P. A.; Düren, T. Elucidating the Breathing of the Metal-Organic Framework MIL-53(Sc) with Ab Initio Molecular Dynamics Simulations and in situ X-Ray Powder Diffraction Experiments. *J. Am. Chem. Soc.* **2013**, *135*, 15763–15773.

(29) Shang, J.; Li, G.; Webley, P. A.; Liu, J. Z. A Density Functional Theory Study for the Adsorption of Various Gases on a Caesium-Exchanged Trapdoor Chabazite. *Comput. Mater. Sci.* **2016**, *122*, 307–313.

(30) Łozińska, M. M.; Mowat, J. P. S.; Wright, P. A.; Thompson, S. P.; Jorda, J. L.; Palomino, M.; Valencia, S.; Rey, F. Cation Gating and Relocation during the Highly Selective "Trapdoor" Adsorption of CO_2 on Univalent Cation Forms of Zeolite Rho. *Chem. Mater.* **2014**, *26*, 2052–2061.

(31) Grand, J.; Barrier, N.; Debost, M.; Clatworthy, E. B.; Laine, F.; Boullay, P.; Nesterenko, N.; Dath, J.-P.; Gilson, J.-P.; Mintova, S. Flexible Template-Free RHO Nanosized Zeolite for Selective CO_2 Adsorption. *Chem. Mater*. **2020**, *32*, 5985–5993.

(32) Taylor, T. C.; Andersson, I. Structural Transitions during Activation and Ligand Binding in Hexadecameric Rubisco Inferred from the Crystal Structure of the Activated Unliganded Spinach Enzyme. *Nat. Struct. Biol*. **1996**, *3*, 95–101.

(33) McDonald, T. M.; Mason, J. A.; Kong, X.; Bloch, E. D.; Gygi, D.; Dani, A.; Crocellà, V.; Giordanino, F.; Odoh, S. O.; Drisdell, W. S.; Vlaisavljevich, B.; Dzubak, A. L.; Poloni, R.; Schnell, S. K.; Planas, N.; Lee, K.; Pascal, T.; Wan, L. F.; Prendergast, D.; Neaton, J. B.; Smit, B.; Kortright, J. B.; Gagliardi, L.; Bordiga, S.; Reimer, J. A.; Long,

J. R. Cooperative Insertion of CO_2 in Diamine-Appended Metal-Organic Frameworks. *Nature* **2015**, *519*, 303–308.

(34) Mao, V. Y.; Milner, P. J.; Lee, J. H.; Forse, A. C.; Kim, E. J.; Siegelman, R. L.; McGuirk, C. M.; Porter-Zasada, L. B.; Neaton, J. B.; Reimer, J. A.; Long, J. R. Cooperative Carbon Dioxide Adsorption in Alcoholamine- and Alkoxyalkylamine-Functionalized Metal–Organic Frameworks. *Angew. Chem. Int. Ed*. **2020**, *59*, 2–12.

(35) Darunte, L. A.; Oetomo, A. D.; Walton, K. S.; Sholl, D. S.; Jones, C. W. Direct Air Capture of CO_2 Using Amine Functionalized MIL-101(Cr). *ACS Sustain. Chem. Eng*. **2016**, *4*, 5761–5768.

(36) Min, J. G.; Kemp, K. C.; Hong, S. B. Zeolites ZSM-25 and PST-20: Selective Carbon Dioxide Adsorbents at High Pressures. *J. Phys. Chem. C* **2017**, *121*, 3404–3409.

(37) Min, J. G.; Kemp, K. C.; Lee, H.; Hong, S. B. CO_2 Adsorption in the RHO Family of Embedded Isoreticular Zeolites. *J. Phys. Chem. C* **2018**, *122*, 28815–28824.

(38) Łozińska, M. M.; Mangano, E.; Mowat, J. P. S.; Shepherd, A. M.; Howe, R. F.; Thompson, S. P.; Parker, J. E.; Brandani, S.; Wright, P. A. Understanding Carbon Dioxide Adsorption on Univalent Cation Forms of the Flexible Zeolite Rho at Conditions Relevant to Carbon Capture from Flue Gases. *J. Am. Chem. Soc*. **2012**, *134*, 17628–17642.

(39) Verbraeken, M. C.; Mennitto, R.; Georgieva, V. M.; Bruce, E. L.; Greenaway, A. G.; Cox, P. A.; Min, J. G.; Hong, S. B.; Wright, P. A.; Brandani, S. Understanding CO2 Adsorption in a Flexible Zeolite through a Combination of Structural, kinetic and Modelling Techniques. *Sep. Purif. Technol*. **2021**, *256*, 117846.

(40) Smith, R. I.; Hull, S.; Tucker, M. G.; Playford, H. Y.; McPhail, D. J.; Waller, S. P.; Norberg, S. T., The Upgraded Polaris Powder Diffractometer at the ISIS Neutron Source, *Rev. Sci. Instrum*. **2019**, *90*, 115101

(41) Coelho, A. TOPAS-Academic; Coelho Software: Brisbane, Australia, 2016.

(42) Larson, A. C.; von Dreele, R. B. GSAS, General Structure Analysis System, Los Alamos National Laboratory, Los Alamos, NM, 1986

(43) Toby, B. H., EXPGUI. A Graphical User Interface for GSAS, J. Appl. Cryst. **2001**, *34*, 210-213.

(44) Dassault Systèmes BIOVIA Materials Studio 2020. Dassault Systèmes: San Diego 2020.

(45) Smith, L. J.; Eckert, H.; Cheetham, A. K. Potassium Cation Effects on Site Preferences in the Mixed Cation Zeolite Li, Na-Chabazite. *Chem. Mater*. **2001**, *13*, 385–391.

(46) Newsam, J. M.; Jarman, R. H.; Jacobson, A. J. A Study of the Mixed $Na_{1-x}Li_x$ Zeolite A System by Powder X-Ray Diffraction. *J. Solid State Chem*. **1985**, *58*, 325–334.

(47) Johnson, G. M.; Reisner, B. A.; Tripathi, A.; Corbin, D. R.; Toby, B. H.; Parise, J. B. Flexibility and Cation Distribution upon Lithium Exchange of Aluminosilicate and Aluminogermanate Materials with the RHO Topology. *Chem. Mater*. **1999**, *11*, 2780–2787.

(48) Millange, F.; Guillou, N.; Walton, R. I.; Grenèche, J. M.; Margiolaki, I.; Férey, G. Effect of the Nature of the Metal on the Breathing Steps in MOFs with Dynamic Frameworks. *Chem. Commun*. **2008**, 4732–4734.

(49) Mowat, J. P. S.; Miller, S. R.; Slawin, A. M. Z.; Seymour, V. R.; Ashbrook, S. E.; Wright, P. A. Synthesis, Characterisation and Adsorption Properties of Microporous Scandium Carboxylates with Rigid and Flexible Frameworks. *Microporous Mesoporous Mater*. **2011**, *142*, 322–333.

(50) Bieniok, A.; Bürgi, H.-B. Deformation Analysis of the D8R-Unit in Zeolite Structures. In Studies in Surface Science and Catalysis; Weitkamp, J., Karge, H. G., Pfeifer, H., Hölderich, W., Eds.; Elsevier B.V.: Amsterdam, **1994**; Vol. 84, pp 567–574.

(51) Cook, M.; Conner, W. C. How Big Are the Pores of Zeolites? In Proceedings of the 12th International Zeolite Conference; Treacy, M. M. J., Marcus, B. K., Bisher, M. E., Higgins, J. B., Eds.; Materials Research Society: Warrendale, PA, USA, **1999**; pp 409–414.

(52) Awati, R. V.; Ravikovitch, P. I.; Sholl, D. S. Efficient and Accurate Methods for Characterizing Effects of Framework Flexibility on Molecular Diffusion in Zeolites: CH_4 Diffusion in Eight Member Ring Zeolites. *J. Phys. Chem. C* **2013**, *117*, 13462–13473.

(53) Pakhomova, A. S.; Danisi, R. M.; Armbruster, T.; Lazic, B.; Gfeller, F.; Krivovichev, S. V.; Yakovenchuk, V. N. High-Temperature Induced Dehydration, Phase Transition and Exsolution in Amicite: A Single-Crystal X-Ray Study. *Microporous Mesoporous*

Mater. **2013**, *182*, 207–219.

(54) Balestra, S. R. G.; Hamad, S.; Ruiz-Salvador, A. R.; Domínguez-García, V.; Merkling, P. J.; Dubbeldam, D.; Calero, S. Understanding Nanopore Window Distortions in the Reversible Molecular Valve Zeolite RHO. *Chem. Mater*. **2015**, *27*, 5657–5667.

(55) Mace, A.; Hedin, N.; Laaksonen, A. Role of Ion Mobility in Molecular Sieving of CO_2 over N_2 with Zeolite NaKA. J. Phys. Chem. C 2013, 117, 24259–24267.

(56) Coudert, F.-X.; Kohen, D. Molecular Insight into CO_2 'Trapdoor' Adsorption in Zeolite Na-RHO, *Chem. Mater*. **2017**, *29*, 2724–2730.

(57) Rzepka, P.; Bacsik, Z.; Pell, A. J.; Hedin, N.; Jaworski, A. Nature of Chemisorbed CO_2 in Zeolite A. *J. Phys. Chem. C* **2019**, *123*, 21497–21503.

(58) Liu, Q.; Pham, T.; Porosoff, M. D.; Lobo, R. F. ZK-5: A CO_2-Selective Zeolite with High Working Capacity at Ambient Temperature and Pressure. *ChemSusChem* **2012**, *5*, 2237–2242.

(59) Georgieva, V. M.; Bruce, E. L.; Chitac, R. G.; Lozinska. M. M.; Hall, A. M.; Murray, C.; Smith, R. I.; Turrina, A.; Wright, P. A. **2021**. Cation Control of Cooperative CO_2 Adsorption in Li-containing Mixed Cation Forms of the Flexible Zeolite Merlinoite (dataset). Dataset. University of St Andrews Portal. https://doi.org/10.17630/cac904b4-3c07-4159-913f-80ff53b13bb7

Graphical Abstract

Cation Control of Cooperative CO_2 Adsorption in Li-containing Mixed Cation forms of the Flexible Zeolite Merlinoite